Journal of Materials Chemistry A

ROYAL SOCIETY OF CHEMISTRY

PAPER

View Article Online
View Journal | View Issue

Cite this: J. Mater. Chem. A, 2026, 14, 11456

Noble-metal-free metal hydroxide Co-catalyst coupled Mn(II)-doped CdS nanorods with bridged charge transport for enhanced photocatalytic hydrogen generation

Walker MacSwain, [b] Xia Hu,*[a] Rongzhen Wu, [c] Zhi-Jun Li, [b] Vanshika Vanshika,[b] De-Kun Ma,[d] Ou Chen [c] and Weiwei Zheng *[b]

Clean and renewable energy from sunlight utilization offers significant opportunities for addressing ongoing energy and environmental crises. In this work, Mn(II) doped 1-dimensional (1D) CdS nanorods (NRs) modified with metal hydroxides ($M(OH)_x$, M = Ni^{2+}, Co^{2+}, and Fe^{3+}) were synthesized as noble metal free photocatalysts for hydrogen generation from water splitting. The incorporation of Mn(II) dopants inside the CdS NRs with a longer lifetime (~ms) than that of the host CdS (~ns) leads to efficient charge separation and subsequent electron transfer, which is more efficient due to the longer lifetime Mn(II) dopants, to $M(OH)_x$ results in higher photocatalytic activity towards water splitting. Interestingly, $Ni(OH)_2$ has the highest efficiency towards photocatalysis under neutral conditions (2.1 fold increase), while the other $M(OH)_x$ (M = Co^{2+} and Fe^{3+}) decorated NRs utilized higher pH values (>13, 2.9 and 2.2 fold increase, respectively) for increased photocatalysis. This can be understood through the changing stable phase in a potential/pH diagram (Pourbaix diagram); at higher pH values, the stable phase of $Ni(OH)_2$ is $Ni(OH)_3^-$ which has a Coulombic repulsive force lowering the ability of photoexcited electrons to transfer to the co-catalytic surface for photo–redox reactions. Enhanced charge transport from a small number of Mn(II) dopants (~0.9% Mn dopants in a CdS NR) efficiently results in increased photocatalysis for the resulting Mn:CdS-$M(OH)_x$ NRs.

Received 2nd November 2025
Accepted 26th January 2026

DOI: 10.1039/d5ta08886k

rsc.li/materials-a

Introduction

The ongoing environmental and energy crises require clean, green energy solutions to alleviate issues stemming from improper renewable resource utilization. Quantum confined semiconductor nanocrystals (NCs), such as CdSe[1–3] and CdS,[4–6] are often utilized as photocatalysts due to their excellent optoelectronic properties including large absorption extinction coefficients in the visible range, size-tunable bandgaps, and shape-dependent charge polarizations across the unconfined axis/axes.[6–9] Altering the morphology of a CdS-based semiconductor, to a 1D CdS nanorod (NR)[10] (unconfined across 1 axis) or a 2D nanoplatelet (unconfined across 2 axes),[11] allows photoexcited electrons to travel, increasing the possibility of an exciton diffusing away from its localized hole pair leading to increased photocatalytic redox activity.[12] However, CdS, like many other semiconductor NCs, suffers from rapid charge recombination (~ns) which is both significantly slower than that of surface reactions (~ms to s)[9,13–15] and has therefore limited charge carriers available to partake in photocatalytic redox reactions.

To overcome this limitation, co-catalysts have been added to CdS-based hybrid semiconductor nanostructures.[6] The co-catalysts can provide electron transfer and/or energy transfer to Fermi energy level of active sites for efficient surface redox reactions. Common co-catalyst utilization can either come as a semiconductor such as TiO_2,[16–18] ZnO,[19–21] CeO_2 [22,23] *etc.*, or as a metal such as Pt[11,24,25] and Au,[17,26,27] *etc.* Co-catalysts provide active sites that facilitate the migration and accumulation of photogenerated electrons and/or holes, thereby enhancing charge separation, prolonging the lifetime of charge-separated states, and promoting efficient surface redox reactions.[24,28–30] Co-catalytic active sites also enhance stability as photocatalysis on the surface of CdS can result in photo-degradation and the formation of SO_4^{2-} on the surface of CdS which poisons the photocatalyst.[31–33]

While noble metals have often been reported for their excellent photocatalytic properties for hydrogen reduction, they are often extremely expensive, which makes their widespread utilization challenging. Therefore, significant efforts have been

[a]School of Life and Environmental Sciences, Shaoxing University, Shaoxing, 312000, P. R. China. E-mail: huxia1111@usx.edu.cn
[b]Department of Chemistry, Syracuse University, Syracuse 13244, New York, USA. E-mail: wzhen104@syr.edu
[c]Department of Chemistry, Brown University, Providence, Rhode Island, 02912, USA
[d]Zhejiang Key Laboratory of Functional ionic membrane Materials and Technology for Hydrogen Production, Shaoxing University, Shaoxing 312000, China

made to replace noble metals with low-cost alternatives, particularly earth abundant first row transition metals such as Ni, Co, and Fe.[34–45] However, first row transition metals are fairly unstable in their metallic forms and often undergo oxidation state changes, such as Ni^{2+} to Ni^{+} under common photocatalytic conditions. Therefore, one such solution to controlling the oxidation state is to form more stable transition metal oxides and/or hydroxides.[34–38,40–44] Metal hydroxides, $M(OH)_x$, offer a low-cost alternative to noble metals while having a relative inexpensiveness and high electron transfer ability with low hydrogen production overpotential.[36,46–52]

Several metal hydroxides such as $Ni(OH)_2$ and $Co(OH)_2$ have been utilized as co-catalysts with CdS-based nanohybrids. A proposed mechanism is electron transfer from CdS to reduce the metal of the metal hydroxides (*i.e.*, Ni^{2+} to Ni^0 metal) for photocatalysis, followed by regeneration of the metal hydroxide as the redox active species takes the electron from the reduced metal.[53] Furthermore, $Ni(OH)_2$ has been noted for its ability to weaken the H–O bond in water for increased H_2 evolution.[35,53,54] Additional approaches to utilizing CdS and $Ni(OH)_2$ nanohybrids are to physically separate the CdS and $Ni(OH)_2$ NPs with reduced graphene oxide to prevent NP agglomeration and increase photocatalytic hydrogen generation.[43] $Ni(OH)_2/Fe(OH)_x$ 0D NPs have been formed on 1D CdS NRs for enhanced photocatalytic hydrogen generation due to the Fe acting as a redox mediator for the redox cycle at the Ni active site.[44] Cobalt hydroxides have also been utilized as co-catalysts with CdS providing enhanced photocatalytic hydrogen generation rates due to its ability to act as an electron acceptor and active site.[51,55] Interestingly, previous work has noted $Co(OH)_2$ NPs as hole trapping sites in their photocatalytic systems for CO_2 reduction.[52] The use of metal hydroxides as co-catalysts is a desirable field of study due to the relative abundance of the first row transition metals and hydroxides coupled with their ability to act as an active site for photocatalysis. However, generally, lower photocatalytic performance of $Ni(OH)_2$ and $Co(OH)_2$ co-catalyst decorated CdS occurs when compared to Pt and other noble metals. This likely is due to (1) stability issues present in transition metal active sites arising from the ease of oxidation state changes, and (2) less efficient electron transfer from CdS to the co-catalyst when comparing conductive noble metals with semiconductor transition metal hydroxides.

The use of dopants can offer an additional relaxation pathway by creating long-lived excitons through host-to-dopant energy transfer. Mn(II) dopants introduce discrete atomic energy levels ($^4T_1$ and $^6A_1$) within the band gap of CdS. The spin-forbidden d–d transition produces an orange emission centered at ~600 nm with a long lifetime (~ms),[12,56–66] which is close to the timescale of surface photocatalytic reactions (~ms–s).[12] Mn dopants in NCs have been utilized as energy transfer donors by transferring energy to Pt co-catalysts for singlet oxygen generation.[67] Based on our previous study, Mn dopants can also act as a bridge between CdS and Pt, funnelling excitons from CdS to the Pt co-catalyst for enhanced photocatalytic redox activity.[12] Therefore we hypothesize that the use of Mn(II) dopants could also act as a bridge between CdS and noble metal free, earth abundant metal hydroxides ($M(OH)_x$) photocatalysts. In this report, we utilized Mn(II) dopants in 1D CdS NRs which were

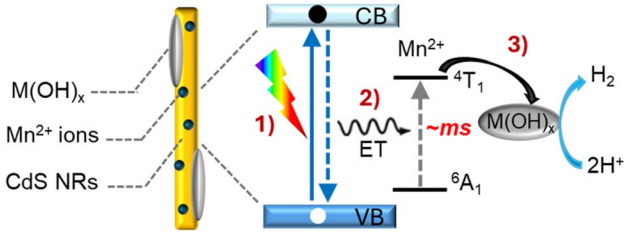

Scheme 1 Schematic illustration of the excitonic and energy transfer processes in Mn(II) doped CdS NRs decorated with $M(OH)_x$ ($M = Ni^{2+}$, Co^{2+}, and Fe^{3+}) for H_2 generation. It should be noted the Mn^{2+} ions are oversized for clarity. (1) Photoexciting an electron from the valence band (VB) to the conduction band (CB), (2) energy transfer (ET) from the host CdS NR to Mn^{2+} dopants, and (3) electron transfer from dopants (with ~ms lifetime) to active sites of $M(OH)_x$ ($M = Ni^{2+}$, Co^{2+}, and Fe^{3+}) for H_2 generation from water splitting.

then decorated with metal hydroxides, $M(OH)_x$ ($M = Ni^{2+}$, Co^{2+}, and Fe^{3+}), (*i.e.*, Mn:CdS-$Ni(OH)_2$, Mn:CdS-$Co(OH)_2$, and Mn:CdS-$Fe(OH)_3$, respectively), for photocatalysis (Scheme 1).

Upon the addition of metal hydroxides to the CdS NRs, the photocatalytic hydrogen generation under blue light irradiation increased by 52 times (52.1 *vs.* 1.0 mmol g^{-1} h^{-1}, pH = 7), 2.5 times (20.5 *vs.* 8.2 mmol g^{-1} h^{-1}, pH > 13), and 3.1 times (25.4 *vs.* 8.2 mmol g^{-1} h^{-1}, pH > 13) for CdS-$Ni(OH)_2$, CdS-$Co(OH)_2$, and CdS-$Fe(OH)_3$, respectively. Aided by the ~1.0 ms lifetime of the excited electrons associated with the Mn(II) dopants, adding $M(OH)_x$ to the Mn:CdS NRs further enhanced the photocatalytic hydrogen yield by 2.1 times (112.0 mmol g^{-1} h^{-1}), 2.9 times (59.5 mmol g^{-1} h^{-1}), and 2.2 times (56.1 mmol g^{-1} h^{-1}), for Mn:CdS-$Ni(OH)_2$ (pH = 7), Mn:CdS-$Co(OH)_2$ (pH > 13), and Mn:CdS-$Fe(OH)_3$ (pH > 13), respectively. The long lifetime of the dopants can increase charge separation and provide a bridging pathway for efficient photocatalysis on $M(OH)_x$ co-catalysts. To the best of our knowledge, this is the first report of noble-metal-free $M(OH)_x$ co-catalyst-modified Mn(II)-doped CdS NRs for photocatalytic hydrogen evolution, and the first demonstration of $Fe(OH)_3$ as an effective co-catalyst in CdS-based hybrid photocatalysts.

Experimental

Chemicals

Cadmium oxide (CdO, ≥99.0%, Sigma-Aldrich), sulfur (99.998%, Sigma-Aldrich), 1-tetradecylphosphonic acid (TDPA, 98%, Sigma-Aldrich), trioctylphosphine oxide (TOPO, 99%, Alfa-Aesar), trioctylphosphine (TOP, 90%, Sigma-Aldrich), chloroform (99.8%, Fisher-Scientific), Mn(II) acetate anhydrous (99.99%, Alfa-Aesar), oleylamine (Oam, 70%, Sigma-Aldrich), oleic acid (OA, 90%, Sigma-Aldrich), 3-mercaptopropionic acid (MPA, 99%, Alfa Aesar), tetramethylammonium hydroxide (TMaOH, 98%, Alfa Aesar), sodium hydroxide (NaOH, 98%, Thermo-Fisher), methanol (≥99%, VWR), toluene (≥99.5%, EMD Chemicals), ethanol (≥99%, anhydrous, Pharmco), acetone (≥99.5%, Sigma-Aldrich), ethyl acetate (≥99%, ACROS), hexane (99%, EMD), isopropyl alcohol (IPA ≥99.5% Sigma-Aldrich), nickel nitrate hexahydrate (99.9985%, STREM), cobalt nitrate hexahydrate (99%, Thermo-Fisher), and ferric

nitrate nonahydrate (98.5%, Fisher-Scientific). Deionized water was used in all experiments. All chemicals were used as purchased without further purification.

Synthesis of 1D CdS NRs

1D CdS NRs were synthesized based on a slightly modified literature reference.[68] Cadmium and sulfur precursor solutions were first prepared separately. The cadmium precursor solution was prepared by mixing 115 mg (0.45 mmol) CdO, 415 mg (0.75 mmol) TDPA, and 3.5 g TOPO in a 50 mL flask and degassing for 1.5 h at 80 °C. The flask was then heated to 340 °C under Ar flow to form a Cd-TDPA complex indicated by a change in solution color from dark red to optically clear and then cooled to 300 °C. The sulfur precursor solution (S-TOP solution) was prepared by dissolving 110 mg (3.4 mmol) of sulfur powder in 10 mL of degassed TOP.

For the synthesis of 1D CdS NRs, 3 mL of the room temperature S-TOP precursor solution was injected into the hot Cd-TDPA solution at 300 °C, and the temperature of the reaction mixture dropped after addition and then ramped back to 300 °C in ~10 min. The remaining S-TOP (~7 mL) solution was injected, 1 mL at a time, every 5 minutes over a 35-minute period, the reaction then proceeded for an additional 30 minutes. At the end of the reaction, the solution was removed from the heating mantle and allowed to cool to approximately 60 °C and then 2–3 mL of chloroform was added to prevent solidification of the crude solution. The CdS NRs were separated from the crude solution by precipitating the particles with ethanol and centrifuging, then dispersed in hexane for optical measurements. The precipitate was further purified once by resuspending the NRs in toluene and then reprecipitating with ethanol and centrifuging for the growth of Pt tips.

Synthesis of 1D Mn:CdS NRs

The Mn(II) dopant precursor (Mn-TOP) was prepared inside a glovebox, where typically, 12 mg (0.04 mmol) of Mn(acetate) anhydrous and 1 mL of TOP were added to a flask. Then the solution was placed under vacuum for 30 minutes. The solution was further sonicated right before use to ensure the Mn(acetate) was fully dissolved.

The synthesis of Mn:CdS NRs followed a similar procedure used for CdS NRs except dropwise addition of the 1 mL Mn-TOP precursor into Cd-TDPA solution at 300 °C and allowed to settle for ~10 minutes. In addition, 9 mL S-TOP (instead of 10 mL S-TOP used in the synthesis of CdS NRs to keep the total volume of the TOP and the reaction the same volume as the undoped CdS NRs) with 2.7 mL of S-TOP is injected first step followed by injecting 0.9 mL every 5 minutes, the reaction then was allowed to proceed for an additional 30 minutes. The same purification method was used as in the undoped CdS NRs.

Ligand exchange

To make water soluble NRs, MPA ligand exchange was performed. Excess amount of MPA (1 mL) was dissolved in 5 mL methanol and the pH of the solution was adjusted to above 12 with TMaOH. The as-synthesized NRs (typically 0.23 mmol) were dispersed in 5 mL hexane and added to the above 5 mL MPA ligand solution in methanol. The solution was stirred overnight in aluminum foil wrapped containers. The MPA capped NRs were precipitated with ethyl acetate and isolated by centrifugation. The precipitate was further purified twice by resuspending the NRs in methanol and then reprecipitating with ethyl acetate and centrifuging.

Synthesis of hybrid 1D Mn:CdS-Ni(OH)$_2$ nanocomposites

The 1D Mn:CdS-Ni(OH)$_2$ hybrid photocatalysts were synthesized according to a modified literature method.[36] First, 0.23 mmol of the ligand exchanged, water soluble CdS NRs were dispersed in 5 mL of 0.05 M NaOH aqueous solution, and then a certain volume of 0.05 M $Ni(NO_3)_2$ aqueous solution (typically, 1.1 mL, 0.055 mmol; molar ratio between CdS : Ni(OH)$_2$ (1 : 0.23) was added dropwise under stirring. The resulting mixture was stirred for a certain amount of time at room temperature (typically one hour). After that, the precipitate was washed three times with deionized methanol and ethyl acetate.

Synthesis of hybrid 1D Mn:CdS-Co(OH)$_2$ nanocomposites

The synthesis of 1D Mn:CdS-Co(OH)$_2$ hybrid photocatalysts followed a modified reported method[51] except the 0.05 M $Ni(NO_3)_2$ aqueous solution is replaced with 0.05 M $Co(NO_3)_2$ aqueous solution, the typical reaction time is raised to three hours, and the typical molar ratio is raised to (1 : 0.25).

Synthesis of hybrid 1D Mn:CdS-Fe(OH)$_3$ nanocomposites

The synthesis of 1D Mn:CdS-Fe(OH)$_3$ hybrid photocatalysts followed the previously mentioned method except the 0.05 M $Ni(NO_3)_2$ aqueous solution is replaced with 0.05 M $Fe(NO_3)_3$ aqueous solution, the typical reaction time is two hours, and the typical molar ratio is changed to (1 : 0.35).

Characterization

Powder X-ray diffraction (XRD) patterns were taken on a Bruker D2 Phaser with a LYKXEYE 1D silicon strip detector using Cu Kα radiation (λ = 1.5406 Å). Transmission electron microscopy (TEM) images and high-resolution (HR-TEM) images were obtained on JEM 2100F (operated at an accelerating voltage of 200 kV). The UV-visible (UV-vis) absorption measurements were collected on an Agilent Cary 60 spectrophotometer. The photoluminescence (PL) measurements were performed with a Horiba FluoroMax Plus spectrofluorometer. Time-resolved emission measurements were conducted using an Edinburgh FLS-980 spectrometer with a photomultiplier tube (PMT, R928 Hamamatsu) detector. For NR bandgap PL lifetime measurements, the pulsed excitation light (365 nm) was used by an Edinburgh EPL-405 pulsed laser diode operating at a repetition rate of 0.2 MHz. For Mn^{2+} emission lifetime measurements, the pulsed excitation light was generated by an μF2 60 W xenon flashlamp operating at a repetition rate of 20 Hz. Elemental composition analysis was performed on a PerkinElmer Avio 220 Max inductively coupled plasma-optical emission Spectrometer (ICP-OES). X-ray photoelectron spectroscopy (XPS) analysis was performed using a Thermo Scientific KAlpha+ instrument

operating on an Al K_α radiation (1486.6 eV). All XPS spectra were calibrated by using the carbon 1s peak at 284.8 eV. Room-temperature X-band EPR spectra were recorded on a Bruker ELEXSYSII E500 spectrometer at a microwave frequency of 9.8 GHz. For electrochemical measurements, a Gamry Interface 1010E electrochemical workstation was used, and the measurements were performed in a three-electrode setup with the sample electrode as the working electrode, platinum wire as the counter electrode, and Ag/AgCl (0.1 M $NaClO_4$, $E_{Ag/AgCl}$ = +0.194 V *vs.* NHE) as the reference electrode. For cyclic voltammetry measurements (CV), a scan rate of 50 mV s^{-1} was utilized over the range of interest. Electrochemical impedance spectra (EIS) were measured in 0.1 M Na_2SO_4 at 1.2 V *vs.* NHE with an amplitude of 25 mV (frequency: 100 mHz–100 kHz) under ambient lighting conditions. The electrochemical electrolyte was degassed for 30 min by flushing with high purity argon prior to CV and EIS measurement. Photocurrent measurements were taken in water at a neutral pH with constant stirring, and a working electrode of FTO glass with an area of 2.4 cm^2. The concentration of the NRs was kept constant by optical absorbance spectroscopy, and the light source was blue light LEDs 405 nm LEDs (λ_{max} = 405 ± 15 nm, 0.675 W).

Photocatalytic generation of hydrogen gas

250 μL (0.009 mg) MPA-ligand exchanged NRs in distilled water, with a stock solution absorbance optical density of 26 at the first exciton peak, were added to a 15 mL glass tube with a stir bar and 2.25 mL distilled water. To each reaction tube, 2.5 mL of isopropyl alcohol was added as a sacrificial hole scavenger. When the pH is kept neutral (pH = 7), 600 μL of DI water were added to the reaction tube, when the pH is adjusted to a basic solution (pH > 13), 600 μL of 0.1 M NaOH were added to the reaction tube. The sample solutions were then vacuumed and refilled with Ar gas. The photochemical reactions were performed in a photochemical reactor equipped with 405 nm LEDs (λ_{max} = 405 ± 15 nm, 0.675 W) under stirring at 1000 rpm which was kept at room temperature by using cold water to prevent heating of the reaction tubes. The volume of the H_2 gas generated was collected in a burette and recorded periodically.

Results

Synthesis and structure of Mn:CdS-M(OH)$_x$ (M = Ni^{2+}, Co^{2+}, and Fe^{3+})

In this study, we synthesized Mn(II) doped 1D CdS NRs decorated with M(OH)$_x$ (*i.e.*, Mn:CdS-M(OH)$_x$ NRs, M = Ni^{2+}, Co^{2+}, and Fe^{3+}) to study the role of dopants and co-catalysts on CdS-based photocatalytic performance. Firstly, 1D Mn:CdS NRs were synthesized *via* a hot-injection method by injecting S-precursor into Cd and Mn-precursor in TOP/TOPO solution at 300 °C. The undoped CdS NRs were also synthesized for comparison with the same procedure without adding the Mn precursor in the reaction. The as-obtained Mn:CdS NRs were then ligand exchanged to be water soluble with 3-mercaptopropionic acid and then decorated with M(OH)$_x$ through M(NO)$_x$ precipitation in deionized water at room temperature.

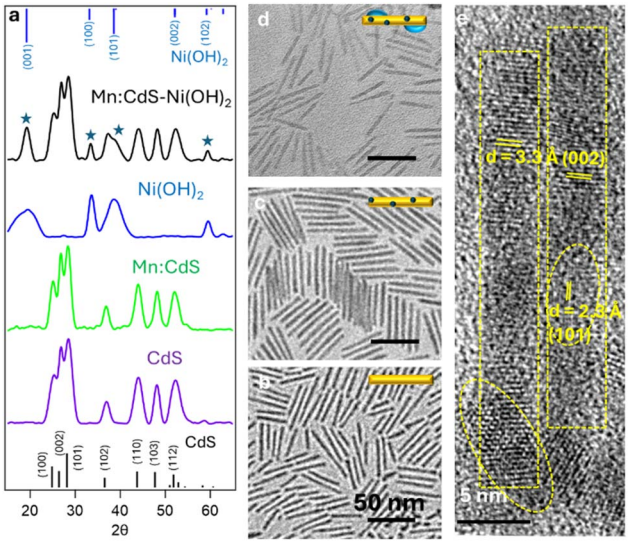

Fig. 1 (a) The X-ray diffraction (XRD) patterns for the CdS, Mn:CdS, and Mn:CdS-Ni(OH)$_2$ NRs. The presence of Ni(OH)$_2$ on Mn:CdS is indicated by a (★). (b) TEM image of CdS NRs, (c) TEM image of Mn:CdS NRs, and (d) TEM image of Mn:CdS-Ni(OH)$_2$ NRs. (e) HR-TEM image of Mn:CdS-NI(OH)$_2$ showing the growth of Ni(OH)$_2$ on the Mn:CdS NRs showing the lattice fringes of CdS (0.33 nm [002] plane of CdS) and Ni(OH)$_2$ (0.23 nm [101] Ni(OH)$_2$). The dotted lines added to draw the viewer's eye.

The structure and morphology of the 1D CdS NR-based photocatalysts were characterized by XRD and TEM. The XRD patterns of the undoped and Mn(II) doped CdS NRs, as well as the Mn:CdS-Ni(OH)$_2$ indicates hexagonal phase 1D CdS NRs (Fig. 1a). The (002) diffraction peak is more intense when compared with the standard hexagonal CdS XRD pattern, indicating cylindric growth of non-spherical NCs along the [001] direction (perpendicular to the (002) plane). After adding Ni(OH)$_2$ to the surface of the Mn:CdS NRs, new XRD peaks are present at 19.2°, 33.4°, ~38.7°, and 59.4° which can be assigned as the (001), (100), (101), and the (102) planes of Ni(OH)$_2$, respectively (Fig. 1a) indicating successful growth of Ni(OH)$_2$ on the Mn:CdS NRs. The XRD patterns of M(OH)$_x$ (M = Co^{2+} and Fe^{3+}) co-catalyst modified NRs are shown in Fig. S2a. After adding either Co(OH)$_2$ or Fe(OH)$_3$ to the surface of the Mn:CdS NRs, however, no significant new XRD peaks are present. This might be due to the small amount of co-catalyst grown on the NRs; a similar lack of XRD patterns are present in previous reports of Co(OH)$_2$ and Fe(OH)$_3$.[69–72]

The TEM images (Fig. 1b and c) show 1D cylindrical CdS and Mn:CdS NRs with average diameter of 4.1 ± 0.5 nm and 4.0 ± 0.5 nm, and an average length of 65 ± 10 nm and 65 ± 10 nm, respectively (Fig. S1). Based on the TEM images and histogram analysis there is no significant difference in either the diameter and/or the length of the NRs with the addition of Mn(II) dopants. The TEM image of Mn:CdS-Ni(OH)$_2$ indicates the growth of the Ni(OH)$_2$ islands on the surface of the Mn:CdS NR (Fig. 1d and e). The HR-TEM image of the Mn:CdS-Ni(OH)$_2$ (Fig. 1e) shows a lattice fringe of 0.33 nm from the CdS NR, consistent with the (100) plane of hexagonal CdS, while the Ni(OH)$_2$ shows a lattice fringe of 0.23 nm consistent with the

(101) plane of $Ni(OH)_2$. Due to the growth of $Ni(OH)_2$ onto the surface of the CdS NRs, the NRs are less uniform in diameter with a larger size distribution (4.0 ± 1.0 nm).

The TEM images of Mn:CdS-$M(OH)_x$ (M = Co^{2+} and Fe^{3+}) indicate successful growth of $M(OH)_x$ on the surface of the Mn:CdS NRs (Fig. S2b and c). The HR-TEM images show a clear lattice fringe of 2.3 Å and 2.4 Å for $Co(OH)_2$ and $Fe(OH)_3$, respectively (Fig. S2d and e) corresponding to the (101) planes of $Fe(OH)_3$ and $Co(OH)_2$ (Fig. S2a). The presence of the CdS (3.3 Å) NRs is also indicated by the HR-TEM lattice fringe for each sample further suggesting successful Mn:CdS-$M(OH)_x$ (M = Co^{2+} and Fe^{3+}) formation.

ICP-OES measurements determined the concentration ratio between Ni and Cd for Mn:CdS-$Ni(OH)_2$ NRs and, a proxy for the concentration of $Ni(OH)_2$ and CdS, to be 0.11 : 1 indicating that roughly half the $Ni(NO_3)_2$ is converted to $Ni(OH)_2$ onto the CdS NRs (Table S1). Similar conversion trends are observed for Mn:CdS-$Co(OH)_2$ and Mn:CdS-$Fe(OH)_3$ NRs with measured ratios of 0.12 : 1 and 0.16 : 1 for $Co(OH)_2$ and $Fe(OH)_3$, respectively on Mn:CdS NRs (Table S1). ICP measurements indicate the same Mn(II) doping efficiency (0.9% Mn dopants) in the $M(OH)_x$ (M = Ni^{2+}, Co^{2+}, and Fe^{3+}) co-catalyst decorated Mn:CdS NRs, which corresponds to ~107 Mn(II) ions per NR.

The survey XPS spectrum (Fig. S3a) of the Mn:CdS NRs shows distinct peaks for Cd 3d, S 2s, and Mn 2p, with the Cd 3d peaks at 406.0 eV ($3d_{5/2}$) and 412.8 eV ($3d_{3/2}$) (Fig. S3e), the S 2p peaks at 162.4 eV ($2p_{3/2}$) and ~163 eV ($2p_{1/2}$) (Fig. S3f), and the Mn(II) dopant peak at 652.3 eV ($2p_{1/2}$) (Fig. S3g), consistent with the literature reported values.[73] Mn:CdS-$M(OH)_x$ NRs (M = Ni^{2+}, Co^{2+}, and Fe^{3+}) have similar peaks present for Mn, Cd, and S (Fig. S3e, g, and f). The Mn:CdS-$Ni(OH)_2$ NRs have new peaks present from $Ni(OH)_2$ with 2p peaks at 861.3 eV and 855.7 eV ($2p_{3/2}$) and 878.1 and 873.4 eV ($2p_{1/2}$) (Fig. S3b), the Mn:CdS-$Co(OH)_2$ NRs have new peaks present from $Co(OH)_2$ with 2p peaks at 789.3 eV and 782.1 eV ($2p_{3/2}$) and 807.1 and 799.8 eV ($2p_{1/2}$) (Fig. S3c), and the Mn:CdS-$Fe(OH)_3$ NRs have new peaks present from $Fe(OH)_3$ with 2p peaks at 789.3 eV and 782.1 eV ($2p_{3/2}$) and 807.1 and 799.8 eV ($2p_{1/2}$) (Fig. S3d), which are consistent with literature reported values.[74–78] The Mn, Cd, and S peaks exhibit a small peak shift (0.5 ± 0.1 eV for Mn $2p_{1/2}$, 0.3 ± 0.1 eV for Cd $3d_{5/2}$ and $3d_{3/2}$, and 0.2 ± 0.1 eV for S $2p_{3/2}$) when comparing the Mn:CdS NRs with the $M(OH)_x$ decorated Mn:CdS NRs, which indicates that the electrons in both the CdS host CB and the Mn^{2+} dopant energy level are interacting with the $M(OH)_x$. As the distance between the Cd $3d_{5/2}$ and Cd $3d_{3/2}$ peaks stays consistent at 6.8 eV, this is further indication that electrons are transferring from the Mn:CdS NRs to the noble metal free $M(OH)_x$ co-catalysts.[12]

Optical properties

Fig. 2a shows the absorption (dotted lines) and emission (solid lines) spectra of the 1D CdS, Mn:CdS, Mn:CdS-$Ni(OH)_2$, Mn:CdS-$Co(OH)_2$, and Mn:CdS-$Fe(OH)_3$ NRs. The first exciton absorption peak for all NRs is at ~470 nm from CdS, corresponding to a 2.6 eV bandgap. For CdS and Mn:CdS NRs, the CdS bandgap PL is at 480 nm and a broad defect emission peak centered around

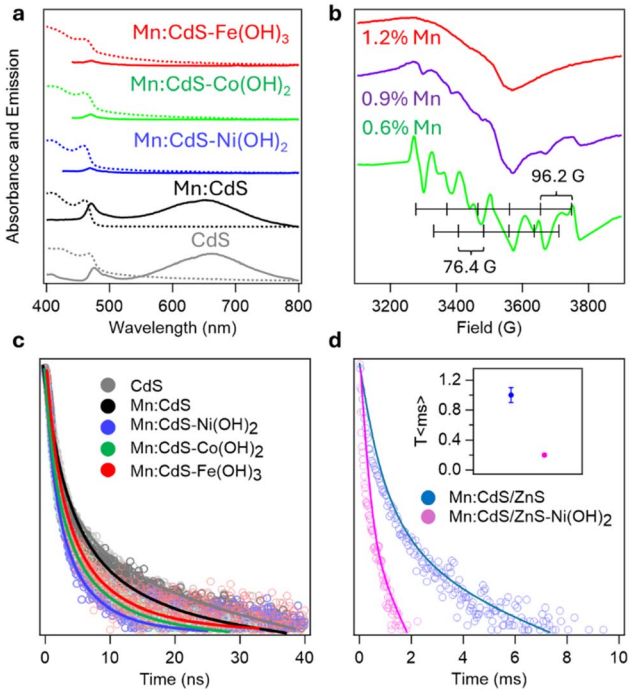

Fig. 2 (a) The absorption (dotted line) and emission (solid line) spectra for the CdS, Mn:CdS, Mn:CdS-$Ni(OH)_2$, Mn:CdS-$Co(OH)_2$, and Mn:CdS-$Fe(OH)_3$ NRs. (b) EPR spectra of the 0.6%, 0.9%, and 1.2% Mn doped CdS NRs showing two sets of hyperfine peak splitting values with 96.2 G for surface Mn and 76.4 G for core Mn. (c) Band edge PL lifetime emission spectra for CdS, Mn:CdS, Mn:CdS-$Ni(OH)_2$, Mn:CdS-$Co(OH)_2$, and Mn:CdS-$Fe(OH)_3$ NRs. (d) PL Mn lifetime emission spectra for core/shell Mn:CdS/ZnS and Mn:CdS/ZnS-$Ni(OH)_2$ NRs.

~650 nm is also present, with PL QYs of 6.3% and 7.4%, respectively. There is no clear Mn(II) emission (~600 nm) present in the Mn:CdS NRs, which might be due to the large amount of surface trapping states considering the large surface to volume ratio of a 1D NR. The PL for Mn:CdS-$Ni(OH)_2$, Mn:CdS-$Co(OH)_2$, and Mn:CdS-$Fe(OH)_3$ does not have a clear emission showing the electron transfer from Mn:CdS to $M(OH)_x$ (M = Ni^{2+}, Co^{2+}, and Fe^{3+}) and PL QY decreases to <1% for each NR (Fig. 2a).

The lifetimes for the CdS band edge PL at ~480 nm of the NRs are shown in Fig. 2c: 5.6 ns for CdS, 4.9 ns for Mn:CdS, 1.9 ns for Mn:CdS-$Ni(OH)_2$, 2.6 ns for Mn:CdS-$Co(OH)_2$, and 2.8 ns for Mn:CdS-$Fe(OH)_3$ NRs (Fig. 2c and Table S2). Compared with undoped CdS NRs, the shorter band-edge PL lifetime observed for Mn:CdS NRs (5.6 ns *vs.* 4.9 ns, Fig. 2c) is attributed to host-to-Mn(II) dopant energy transfer, which introduces an additional relaxation pathway for photogenerated charge carriers (Scheme 1). To reveal if there is direct electron transfer from Mn dopants to $M(OH)_x$ co-catalysts, the lifetimes for the $M(OH)_x$ decorated undoped NRs (*i.e.*, CdS-$M(OH)_x$ (M = Ni^{2+}, Co^{2+}, and Fe^{3+}) were measured, which show lifetime of 3.6 ns for CdS-$Ni(OH)_2$, 4.2 ns for CdS-$Co(OH)_2$, and 4.3 ns for CdS-$Fe(OH)_3$ (Fig. S4 and Table S1, see SI for information on synthesis and characterization details). The further decrease in the band edge PL lifetime when comparing the $M(OH)_x$ decorated undoped CdS NRs (3.6–4.3 ns) with the lifetimes of their Mn doped counterparts (1.9–2.8 ns), suggests the additional Mn(II) to

$M(OH)_x$ relaxation pathway by electron transfer (Fig. 2c and Table S2). Therefore, the Mn(II) dopants with longer PL lifetime (Fig. 2d) could enhance the electron transfer from the 1D CdS NRs to $M(OH)_x$.

The presence of Mn(II) dopants within the CdS host lattice was also confirmed by X-band EPR spectroscopy (Fig. 2b). In the Mn:CdS NRs, there are two sets of six-peak hyperfine splitting patterns with hyperfine constants (A) of 96.2 and 76.4 G, corresponding to the Mn(II) ions on the surface and the core of the CdS lattice, respectively. As the ICP measured concentration of the Mn(II) dopants increases from 0.9% to 1.2% (Fig. 2b) the hyperfine peaks splitting patterns are less pronounced and eventually lost due to the concentration quenching effect.[79–81]

To better observe the Mn dopant emission (~600 nm) and determine the lifetime of the excited electrons associated with Mn(II) dopants, control experiments of a ZnS surface passivated Mn:CdS NRs and Mn:CdS/ZnS-$Ni(OH)_2$ NRs were performed to remove surface defects and therefore the broad surface defect emission (~650 nm). The resulting core/shell Mn:CdS/ZnS NRs show a clear Mn(II) dopant emission at ~600 nm (Fig. S5a), however, the emission intensity is diminished upon the addition of $Ni(OH)_2$ (Fig. S5a, see SI for information on synthesis and characterization details).

The Mn(II) emission lifetime from the Mn:CdS/ZnS core/shell NRs is ~1.0 ms, which decreases to ~0.2 ms upon $Ni(OH)_2$ decoration in the Mn:CdS/ZnS-$Ni(OH)_2$ NRs (Fig. 2d). The pronounced decrease in Mn(II) emission lifetime upon deposition of $Ni(OH)_2$ further indicates electron transfer from Mn(II) dopant states to the co-catalyst in the hybrid nanostructures. A similar charge-transfer pathway is expected for $Co(OH)_2$- and $Fe(OH)_3$-decorated Mn:CdS NRs. In addition, after ZnS shell coating, only a singular hyperfine peak splitting pattern is observed of 68 G from the core Mn(II) dopants was observed (Fig. S5c), which proves the smaller EPR hyperfine splitting (76.4 G) arising from the core Mn(II) ions in CdS NRs.

Electrochemical properties

The charge transport resistance is a facsimile for the availability of electrons to participate in photocatalytic redox reactions, and therefore, the charge transport properties of the as-synthesized NRs were studied by electrochemical impedance spectroscopy (EIS). In the EIS spectra, the smaller the semicircle arc, the better the potential for photocatalysis. As shown in Fig. 3a, the Mn:CdS NRs have a smaller semicircle arc than CdS, demonstrating decreased charge transfer resistance for Mn:CdS NRs compared to CdS NRs, suggesting that the long-lived Mn(II) dopants are altering the charge recombination dynamics and allowing more electrons to participate in photocatalysis.

For comparison, Mn(II) doped and undoped CdS NRs decorated with $M(OH)_x$ ($M = Ni^{2+}$, Co^{2+}, and Fe^{3+}) were synthesized and the corresponding EIS plots are shown in Fig. 3b. Further reduction of the charge transport resistance (smaller semicircle arc) was obtained by the growth of $M(OH)_x$ islands on the Mn:CdS NRs (Fig. 3a and b), with a general trend of $Ni(OH)_2$ < $Co(OH)_2$ < $Fe(OH)_3$ showing that $Ni(OH)_2$ is expected to give the largest photocatalysis followed by $Co(OH)_2$ and then $Fe(OH)_3$. Furthermore, decreased charge transport resistance from Mn:CdS-$M(OH)_x$ NRs suggests that the Mn(II) dopants can interact with $M(OH)_x$ co-catalysts for enhanced photocatalysis. The as-calculated values for R_s and R_{ct} for the NR photocatalysts (Table S3) show the decreased charge transfer resistance for the CdS-based NRs upon the addition of Mn(II) dopants.

Cyclic voltammetry (CV) was used to study the bandgap of the 1D CdS NR-based photocatalysts and thus their suitability for catalytic water reduction (Fig. S6). The position of the conduction band can be measured by finding the onset of the current increase on the CV which occurs at ~−0.8 V *vs.* NHE (Fig. S6). The CdS-based NRs show a bandgap of ~2.6 eV consistent with the absorption data in Fig. 2a.

There is not a significant change in the CV upon the addition of $M(OH)_x$ ($M = Ni^{2+}$, Co^{2+}, and Fe^{3+}) suggesting that the bandgap remains consistent at ~2.6 eV, further confirmed by the absorption data in Fig. 2a and S4a. Therefore, the bandgaps of each CdS-based NR (Fig. S6) are wide enough to cover the 1.23 eV needed to split water and generate hydrogen gas. For the Mn(II) doped NRs, there is an increase in the area under the CV curve at ~0.8 V; this could be attributed to the presence of the Mn^{2+} dopants as the CV measures the available states for electrons to be added. The $M(OH)_x$ NRs have a peak at roughly −0.4 V, −0.5 V, and −0.7 V for the $Ni(OH)_2$, $Co(OH)_2$, and $Fe(OH)_3$ decorated NRs, respectively, which can be attributed to the reduction process of forming Ni(0), Co(0), and Fe(0) metal, respectively.[72,82–85]

Photocurrent measurements were performed for the CdS-based NRs (Fig. 3c). The transient photocurrent responses

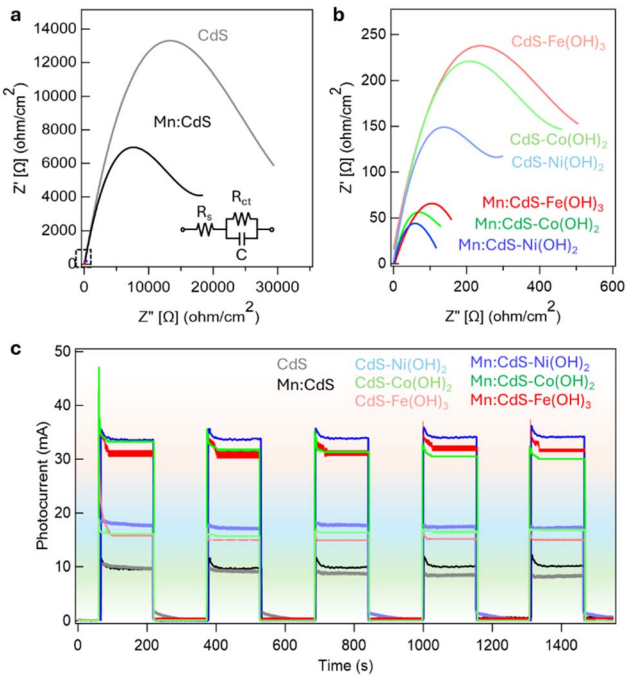

Fig. 3 (a) EIS spectra for CdS, Mn:CdS, CdS-$M(OH)_x$ ($M = Ni^{2+}$, Co^{2+}, and Fe^{3+}), and Mn:CdS-$M(OH)_x$ ($M = Ni^{2+}$, Co^{2+}, and Fe^{3+}) NRs. (b) Zoomed in EIS spectra for the CdS-$M(OH)_x$ ($M = Ni^{2+}$, Co^{2+}, and Fe^{3+}), and Mn:CdS-$M(OH)_x$ ($M = Ni^{2+}$, Co^{2+}, and Fe^{3+}) NRs. (c) Photocurrent measurements of CdS, Mn:CdS, and their corresponding co-catalyst $M(OH)_x$ ($M = Ni^{2+}$, Co^{2+}, and Fe^{3+}) decorated NRs.

increased after the incorporation of Mn(II) dopants into the CdS NRs; there was a further significant photocurrent enhancement after $M(OH)_x$ (M = Ni^{2+}, Co^{2+}, and Fe^{3+}) decoration. This enhancement of the photocurrent response is consistent with the shorter band edge PL lifetime (CdS > Mn:CdS > Mn:CdS-$M(OH)_x$) (Fig. 2c) showing additional electron relaxation pathways to the dopants and co-catalyst. The photocurrent responses also follow a general trend of $Ni(OH)_2$ > $Co(OH)_2$ > $Fe(OH)_3$ in the Mn(II) doped and undoped CdS NRs and is also consistent with the reduced charge transport resistance in Mn:CdS-$M(OH)_x$ NRs from the EIS data (Fig. 3a and b).

Photocatalytic H_2 generation by water splitting

Photocatalytic hydrogen generation from water splitting experiments were conducted with the NRs under blue light LED (λ_{max} = 405 ± 15 nm, 0.675 W) irradiation at room temperature with a neutral pH (pH = 7). Fig. 4 shows the catalytic performance of the 1D CdS NR-based NRs. The CdS NRs generated 0.8 mmol g^{-1} h^{-1} of hydrogen gas, while the Mn:CdS NRs did not show notable hydrogen generation enhancement (1.0 mmol g^{-1} h^{-1}) under the same reaction conditions. This can be explained by the isolated Mn(II) dopants which are (1) not always on the surface of the CdS NRs (see EPR Fig. 2b) and (2) the small portion of surface Mn(II) dopants could not provide enough active sites for water molecules.

Upon the addition of $M(OH)_x$ (M = Ni^{2+}, Co^{2+}, and Fe^{3+}) co-catalysts, significant enhancement of the photocatalysis was achieved compared to the Mn:CdS NRs (1.0 mmol g^{-1} h^{-1}) of 108.2, 17.3, and 13.6 mmol g^{-1} h^{-1} of hydrogen generation for 1D Mn:CdS-$Ni(OH)_2$, Mn:CdS-$Co(OH)_2$, and Mn:CdS-$Fe(OH)_3$ NRs, respectively. In addition, without Mn(II) dopants 52.1, 11.0, and 4.0 mmol g^{-1} h^{-1} of hydrogen gas were generated from the CdS-$Ni(OH)_2$, CdS-$Co(OH)_2$, and CdS-$Fe(OH)_3$ NRs, respectively. Generally, the NRs follow a consistent photocatalytic performance trend of $Ni(OH)_2$ > $Co(OH)_2$ > $Fe(OH)_3$ when comparing the Mn(II) doped NRs with their undoped counterparts (*i.e.*, Mn:CdS-$Ni(OH)_2$ *vs.* CdS-$Ni(OH)_2$); enhanced photocatalysis observed from the Mn(II) doped and/or co-catalyst decorated NRs is consistent with decreased charge transport resistance as measured in the EIS spectra (Fig. 3a and b). Therefore, enhanced hydrogen generation arises from the synergistic effect between long lifetime Mn(II) dopants (~ms) (Fig. 2d) and electron transfer to the co-catalyst resulting in electrons accumulating on the $M(OH)_x$ islands for subsequent photo–redox reactions.

Recycle tests were also performed to study the stability of the photocatalysts, in which the photocatalyst was re-collected and the photocatalytic solution was remade by adding the same amount of hole scavenger at the same pH (Fig. 4e). The hour-by-hour recycling reaction using the same 1D Mn:CdS-$Ni(OH)_2$ photocatalyst revealed a stable ~95% performance of the previous photocatalytic result over the course of three cycles, highlighting the photostable recyclability for the photocatalyst. Recycle tests for Mn(II) doped CdS NRs decorated with $M(OH)_x$ (M = Co^{2+} and Fe^{3+}) were also performed (Fig. 4f and g), showing limited stability during the recycle tests which might be due to the limited stability of $Co(OH)_2$ and $Fe(OH)_3$ in neutral pH during the sample cleaning and recycling processes (see effect of pH in the Discussion section).

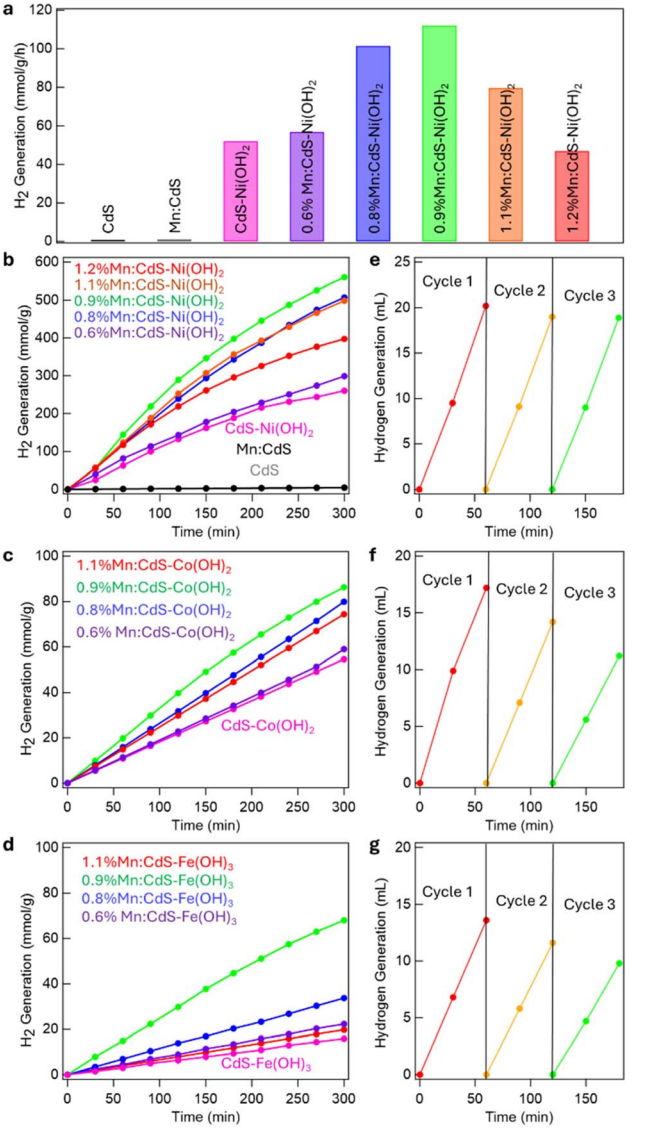

Fig. 4 (a) Average hydrogen generation of the Mn:CdS-$Ni(OH)_2$ NRs in mmol g^{-1} h^{-1}. Photocatalytic hydrogen generation of (b) CdS, Mn:CdS, CdS-$Ni(OH)_2$, and Mn:CdS-$Ni(OH)_2$, (c) CdS-$Co(OH)_2$ and Mn:CdS-$Co(OH)_2$, and (d) CdS-$Fe(OH)_3$ and Mn:CdS-$Fe(OH)_3$ at neutral pH with differing Mn doping concentrations shown as % of Mn atoms per CdS NR. Recycle test for the (e) Mn:CdS-$Ni(OH)_2$ NRs, (f) Mn:CdS-$Co(OH)_2$ NRs, and (g) Mn:CdS-$Fe(OH)_3$ NRs over three one-hour cycles.

Discussion

Photocatalytic mechanism of 1D Mn:CdS-$M(OH)_x$ hybrid NRs

Fig. 5a illustrates the host-to-dopant energy transfer and following electron transport to the $M(OH)_x$ co-catalyst in the 1D Mn:CdS-$M(OH)_x$ (M = Ni^{2+}, Co^{2+}, and Fe^{3+}) NRs for photocatalytic H_2 gas generation under blue light excitation. The interactions between the long lifetime Mn(II) dopants and the

$M(OH)_x$ co-catalyst demonstrates the two-step nature of the charge carrier transport. Firstly, the CdS absorbs light from the photoreactor, then Step 1 host-to-dopant energy transfer occurs creating long-lived lifetimes of the excitons (ms) on the Mn(II) dopants. Step 2 follows where electron transfer from either the host CdS (ns) or Mn(II) dopants (ms), though likely more the Mn(II) dopants due to the difference in photocatalytic hydrogen generation (Fig. 4a–d) and lifetime (Fig. 2c, S4b, and Table S2), to the co-catalyst $M(OH)_x$ for more efficient photocatalysis due to an increase in the lifetimes of the charge separated states.

The shorter CdS PL lifetime of the Mn:CdS NRs compared to that of pristine CdS NRs (Fig. 2c and Table S2) indicates the host-to-dopant energy transfer (Step 1). The following electron transfer (Step 2) from Mn:CdS to $M(OH)_x$ ($M = Ni^{2+}$, Co^{2+}, and Fe^{3+}) is demonstrated by the decrease in PL QY after $M(OH)_x$ decoration (Fig. 2a). In addition, the Mn(II) dopant PL lifetime

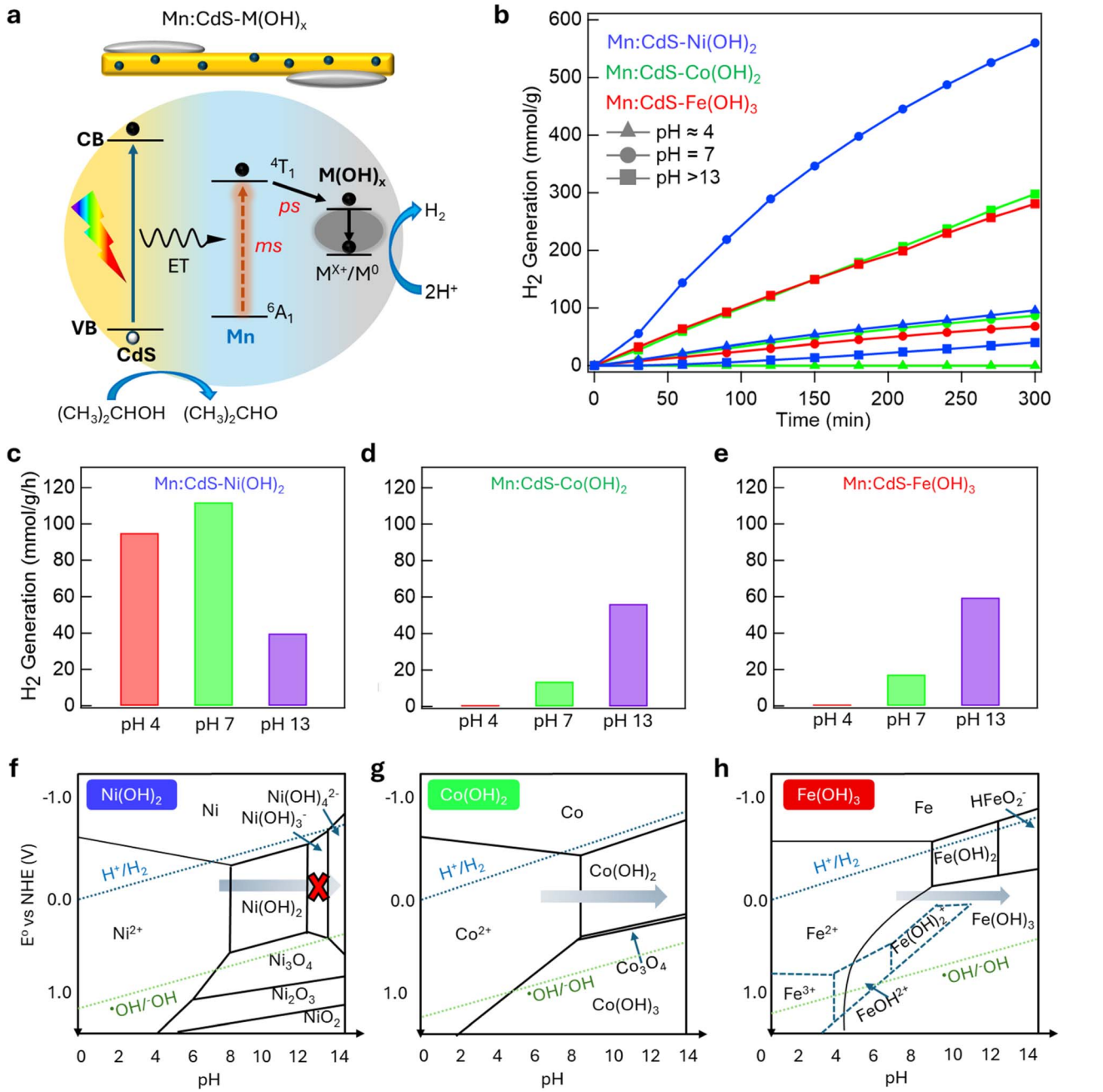

Fig. 5 (a) Schematic illustration of the host-to-dopant energy transfer and following electron transport to the $M(OH)_x$ co-catalyst with subsequent M(*X*) to M(0) ($M = Ni^{2+}$, Co^{2+}, and Fe^{3+}) self-reduction for photocatalytic hydrogen generation from water splitting in the 1D Mn:CdS-$M(OH)_x$ NRs at neutral pH. Note: the Mn^{2+} ions are oversized for clarity. (b) pH dependent photocatalytic hydrogen generation of the Mn:CdS-$M(OH)_x$ ($M = Ni^{2+}$, Co^{2+}, and Fe^{3+}) decorated NRs. pH dependent photocatalysis of the Mn:CdS-$M(OH)_x$ ($M =$ (c) Ni^{2+}, (d) Co^{2+}, and (e) Fe^{3+}) NRs in mmol g^{-1} h^{-1} of hydrogen generated. Pourbaix diagrams[86] showing the electrochemical stability of (f) $Ni(OH)_2$,[87] (g) $Co(OH)_2$,[88,89] and (h) $Fe(OH)_3$.[90,91]

in the Mn:CdS/ZnS type I core/shell NRs also decreases after growth of $Ni(OH)_2$ co-catalyst due to electron transfer from Mn(II) dopants to $Ni(OH)_2$ (Fig. 2d). Further evidence of two successive steps is demonstrated by the reduced charge transport resistance and enhanced charge transport from CdS to Mn:CdS to Mn:CdS-$M(OH)_x$ NRs by EIS data (Fig. 3a and b) and the photocurrent results (Fig. 3c).

The longer lifetime Mn(II) dopants function as a bridge between the light harvesting CdS and active co-catalytic $M(OH)_x$ for enhanced charge transport, which leads to a greater hydrogen generation efficiency. The positions of the band edges of CdS, Mn^{2+} dopants, and the metals Ni(0), Co(0), and Fe(0) (generated from the respective reduction of $M(OH)_x$ ($M = Ni^{2+}$, Co^{2+}, and Fe^{3+}), see below) are more negative *vs.* NHE than the reduction potential of water,[49,50,72,84,85,92–95] where these energy band levels are in a down-stepping structure moving the electrons to the $M(OH)_x$ for photocatalytic hydrogen generation from water splitting (Fig. 5a).

Previous reports propose that $Ni(OH)_2$ undergoes self-reduction during photocatalysis to form isolated Ni(0) atoms/small clusters on the surface of the CdS NR.[49,50] These isolated Ni(0) species act as active sites for hydrogen evolution while $Ni(OH)_2$ improves the mass transport of H_2O to the self-reduced Ni(0).[49,50] This process has also been reported for $Co(OH)_2$ [51] and in this first report of $Fe(OH)_3$ co-catalyst utilization in CdS-based photocatalysts, a similar photocatalytic mechanistic reduction of $Fe(OH)_3$ to Fe(0) is proposed. Therefore, during photocatalysis, reduction of the co-catalyst $M(OH)_x$ to the metallic form occurs *in situ* before photocatalytic interaction with hydrogen in solution (Fig. 5a). It should be noted that at the interface between the CdS semiconductor and the $M(OH)_x$ co-catalyst, Fermi-level equilibration leads to the formation of a Schottky barrier, inducing interfacial band bending and charge redistribution. This interfacial effect promotes efficient charge separation and suppresses recombination of photogenerated carriers.

Effect of pH

The photocatalytic performance of the $Ni(OH)_2$ decorated NRs (Fig. 4a) follow the observed trends in the EIS spectra (Fig. 3b) and PL lifetime (Fig. 2c and S4b), where the greatest photocatalytic performance is expected from Mn(II) doped CdS NRs decorated with $Ni(OH)_2$, then $Co(OH)_2$, and $Fe(OH)_3$ followed by undoped CdS NRs decorated with $Ni(OH)_2$, then $Co(OH)_2$, and $Fe(OH)_3$. However, the Mn:CdS-$M(OH)_x$ ($M = Co^{2+}$ and Fe^{3+}) NRs had lower photocatalytic hydrogen generation than undoped CdS-$Ni(OH)_2$ (Fig. 4), which is inconsistent with the EIS spectra (Fig. 3b) and PL lifetime (Fig. 2c and S6). To understand these observed results, pH dependent photocatalysis of the 0.9% Mn(II) doped CdS $M(OH)_x$ co-catalyst decorated NRs were measured (Fig. 5b).

The highest rate of photocatalysis for the Mn:CdS-$Ni(OH)_2$ NRs was at a neutral pH (pH = 7) (Fig. 5c), while the highest rate of photocatalysis for the Mn:CdS-$Co(OH)_2$ (Fig. 5d) and Mn:CdS-$Fe(OH)_3$ NRs (Fig. 5e) was at a basic pH > 13. A likely explanation for pH-dependent performance is due to the forms of the $M(OH)_x$ are as function of pH, shown in Pourbaix diagram(s) (Fig. 5f, g, and h).[86–91] As the pH grows more basic, the form of $Ni(OH)_2$ that is most stable changes from Ni^{2+} (pH ≈ 4), to $Ni(OH)_2$ (pH = 7), to $Ni(OH)^{3-}$ (pH > 13) (Fig. 5f). However, for $Co(OH)_2$ and $Fe(OH)_3$, the stable form is either Fe^{2+} or Co^{2+}, respectively in acidic (pH ≈ 4) or neutral (pH = 7) conditions, while at more basic conditions (pH > 13), the metal hydroxide is formed for $Fe(OH)_3$ and $Co(OH)_2$, respectively (Fig. 5g and h).

Therefore, the as-observed trends in Fig. 5c–e can be explained by the forms of the transition metal compounds. Both Ni^{2+} [96,97] and $Ni(OH)_2$ [36,43,48,82] are known to undergo photocatalytic hydrogen generation. However, $Ni(OH)_3^-$ has a negative change and would likely have Coulombic repulsion towards any photoexcited electron from Mn:CdS resulting in lower photocatalysis. As $Fe(OH)_3$ and $Co(OH)_2$ are stable at pH > 13 and since IPA hole scavenging is best at basic conditions,[98] the greatest photocatalytic enhancement for Mn:CdS-$Co(OH)_2$ and Mn:CdS-$Fe(OH)_3$ can occur at basic conditions. The lack of a Coulombic repulsive force on these metal hydroxide co-catalysts allows for more efficient electron transfer. This could also explain the lack of recycling stability for the $M(OH)_x$ ($M = Co^{2+}$ and Fe^{3+}) NRs as during the cleaning process, the solutions return to a neutral pH which could start the formation of side products and poison the photocatalyst (Fig. 4f and g).

Fig. 6a and b show the catalytic performance of the NRs under basic conditions for photocatalytic hydrogen generation from water splitting. CdS generated 8.2 mmol g^{-1} h^{-1} of hydrogen gas, Mn:CdS generated 9.8 mmol g^{-1} h^{-1} of hydrogen gas. As IPA hole scavenging is more efficient under basic conditions,[98] the likelihood of Coulombic forces preventing photocatalysis are lessened and therefore, the longer-lived lifetimes arising from Mn(II) dopants can perform better for the Mn:CdS NRs.

At basic pH (>13), the 1D Mn:CdS-$Co(OH)_2$ NRs show an improvement of 3.4 times in overall hydrogen generation when compared with the neutral pH Mn:CdS-$Co(OH)_2$ NRs (59.5 *vs.* 17.3 mmol g^{-1} h^{-1}) (Fig. 4c and 6a). The 1D Mn:CdS-$Fe(OH)_3$ NRs, show an enhanced photocatalytic hydrogen generation of 4.1 times greater than Mn:CdS-$Fe(OH)_3$ at neutral pH (56.1 *vs.* 13.6 mmol g^{-1} h^{-1}) (Fig. 4d and 6b). The increased photocatalytic hydrogen generation for Mn:CdS-$Co(OH)_2$ and Mn:CdS-$Fe(OH)_3$ upon changing the pH (Fig. 5b) from neutral to basic demonstrates the importance of controlling the form of first row transition metal compounds (Fig. 5c–e). At pH values where the $M(OH)_x$ is positive or neutrally charged from the Pourbaix diagrams (Fig. 5f–h), higher photocatalytic hydrogen generation is observed consistent with photocatalytic trends observed for Mn:CdS-$Ni(OH)_2$ (Fig. 4a), Mn:CdS-$Co(OH)_2$ (Fig. 4c and 6a), and Mn:CdS-$Fe(OH)_3$ (Fig. 4d and 6b).

Mn(II) dopant concentration-dependent photocatalytic performance

The role of Mn(II) dopants acting as a bridge between CdS and $M(OH)_x$ was further elucidated by comparing the impact of Mn(II) doping concentration on the CdS NRs. First, a control experiments to determine the photocatalytic hydrogen generation of undoped CdS-$M(OH)_x$ NRs was performed, with 52.1, 20.3, and

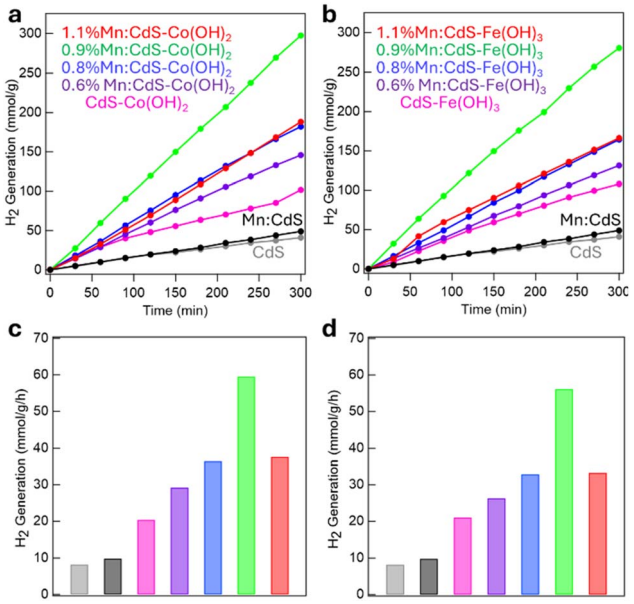

Fig. 6 (a) Photocatalytic hydrogen generation of CdS, Mn:CdS, CdS-$Co(OH)_2$, and Mn:CdS-$Co(OH)_2$ under basic conditions (pH > 13) with differing Mn doping concentrations shown as % of Mn atoms per CdS NR. (b) Photocatalytic hydrogen generation of CdS, Mn:CdS, CdS-$Fe(OH)_3$, and Mn:CdS-$Fe(OH)_3$ under basic conditions (pH > 13) with the Mn doping concentrations shown as % of Mn atoms per CdS NR. Average hydrogen generation of the (c) Mn:CdS-$Co(OH)_2$ and (d) Mn:CdS-$Fe(OH)_3$ NRs in mmol g^{-1} h^{-1}, color coded with the results in (a) and (b).

25.4 mmol g^{-1} h^{-1} of H_2 gas generated on CdS-$Ni(OH)_2$ (Fig. 4a, pH 7), CdS-$Co(OH)_2$ (Fig. 6a, pH > 13), and CdS-$Fe(OH)_3$ NRs (Fig. 6b, pH 13), respectively. To further reveal the Mn dopant-dependent performance of the hybrid catalysts, we also investigated the photocatalysis of Mn:CdS-$M(OH)_x$ with [Mn] between 0.6% and 1.2%. The maximum hydrogen generation yield occurs at 0.9% Mn(II) dopants in $M(OH)_x$ decorated NRs with 112.0, 59.5, and 56.1 mmol g^{-1} h^{-1} for Mn:CdS-$Ni(OH)_2$, Mn:CdS-$Co(OH)_2$, and Mn:CdS-$Fe(OH)_3$, respectively (Fig. 4a and 6a, b).

At Mn(II) concentrations lower than the ideal Mn(II) concentration, there are less than an ideal number of energy transfer acceptors in the host-to-dopant energy transfer system. When the concentration of Mn(II) dopants is either 0.6% or 0.8%, the photocatalytic hydrogen yield is 56.9 and 101.4 mol g^{-1} h^{-1}, for 0.6% and 0.8% Mn doped Mn:CdS-$Ni(OH)_2$; 29.1 and 36.4 mmol g^{-1} h^{-1} for 0.6% and 0.8% Mn doped Mn:CdS-$Co(OH)_2$; and 26.2 and 32.8 mmol g^{-1} h^{-1} for 0.6% and 0.8% Mn doped Mn:CdS-$Fe(OH)_3$, respectively. With limited (<0.9%) Mn(II) dopants available for host-to-dopant energy transfer, fewer excited excitons can transfer their energy to Mn(II) dopants, resulting in a limited increase in the photocatalytic hydrogen generation over pure CdS (Fig. 4a and 6a, b). However, the lifetime of the Mn(II) PL lifetime stays relatively constant from 1.01 to 0.97 ms when the Mn(II) concentration decreases from 0.9% to 0.6% of the corresponding Mn:CdS/ZnS NRs (Fig. S5b) suggesting that any decrease in photocatalysis does not come from a lack of ability of the Mn(II) dopants to effectively promote the lifetime of the charge separated states. Therefore, this highlights the important impact of having enough Mn(II) acceptors for efficient bridging; the severely isolated Mn(II) dopants cannot effectively shuttle electrons from photoexcited CdS to $M(OH)_x$ and as a result, effective photocatalysis cannot occur.

At higher Mn(II) concentrations than the ideal (>0.9%), short-range Mn–Mn interactions lead to a concentration quenching effect, as shown by a broad dipolar EPR peak without well-resolved hyperfine peaks (Fig. 2b). The higher Mn doping concentration leads to reduced hydrogen generation with 1.05% Mn-doped Mn:CdS-$M(OH)_x$ having 79.5, 37.6, and 33.2 mmol g^{-1} h^{-1} for Mn:CdS-$Ni(OH)_2$, Mn:CdS-$Co(OH)_2$, and Mn:CdS-$Fe(OH)_3$, respectively (Fig. 4a and 6a, b) as the concentration quenching reduces the number of long-lived charge carriers from being utilized in photocatalysis. Concentration quenching is common at higher doping concentrations due to the cross-relaxation between Mn–Mn coupled dopants where the dopants are closer to each other.[99,100] The concentration quenching effect can also be seen in the PL lifetime spectra of the Mn(II) doped core/shell Mn:CdS/ZnS NRs as the Mn(II) PL lifetime decreases from 1.01 to 0.87 ms when the Mn(II) concentration increases from 0.9% to 1.2% (Fig. S5b and inset). Since the Mn(II) dopants provide an alternative relaxation pathway for the photoexcited electrons, it can be understood that fewer are available to undergo photocatalysis if concentration quenching occurs.

Decoration of Mn:CdS by $M(OH)_x$

The co-catalyst $M(OH)_x$ (M = Ni^{2+}, Co^{2+}, and Fe^{3+}) on the Mn:CdS-based NRs shows both time and concentration based photocatalytic dependence. In Fig. S7 the hydrogen generation of $M(OH)_x$ at different reaction times is shown. The highest photocatalytic yield is observed for a one-hour reaction of $Ni(OH)_2$, for three hours on $Co(OH)_2$, and three-hours for $Fe(OH)_3$ on Mn:CdS. When the $M(OH)_x$ reaction time is half the ideal reaction time, the photocatalytic yield decreases by ~50%. At reaction times longer one-hour, from 1.5 hours to 7 hours, the photocatalytic hydrogen yield decreases as the reaction time increases until at 420+ minutes, the photocatalytic hydrogen yield even becomes negligible for $M(OH)_x$ (M = Ni^{2+}, Co^{2+}). This can be understood by the reaction time controlling the total decoration of the $M(OH)_x$ on the Mn:CdS NRs. Below the ideal reaction times, not enough $M(OH)_x$ decoration occurs; above the ideal reaction time, too much $M(OH)_x$ growth occurs which likely blocks incident light from reaching CdS and undergoing charge separation for photocatalysis.

There is also a similar $M(OH)_x$ concentration dependent-performance between the Mn:CdS-$Ni(OH)_2$ NRs with differing $M(OH)_x$ concentrations. When the $M(OH)_x$ concentration was varied, the reaction time for the $M(OH)_x$ was kept constant at the respective ideals (1, 3, and 2 hours respectively $Ni(OH)_2$, $Co(OH)_2$, and $Fe(OH)_3$). Fig. S8 shows the molar ratio dependence of the $M(OH)_x$ decoration as measured by ICP (see Table S1 and discussion in results section for more details on the calculation). For example, when the molar ratio between CdS and $Ni(OH)_2$ is less than 1 : 0.23, the rate of photocatalytic hydrogen evolution decreases, while above 1 : 0.23, the rate similarly decreases. This can be understood as at lower $Ni(OH)_2$

concentrations, not enough $Ni(OH)_2$ active sites are present on the surface of CdS. While at higher concentrations of $Ni(OH)_2$, the co-catalyst growth can occur quicker and thus, there is too much $Ni(OH)_2$ decoration which hinders photocatalysis. As this trend remains consistent for $M(OH)_x$ ($M = Co^{2+}$ and Fe^{3+}), a similar conclusion can be made, too much $M(OH)_x$ decoration and the co-catalyst partially blocks incident light Mn:CdS, too little $M(OH)_x$ decoration and there are not enough active sites for photocatalysis.

Conclusions

To overcome the limitation of fast charge recombination of pristine CdS nanomaterials, we have developed noble metal free co-catalyst $M(OH)_x$ ($M = Ni^{2+}$, Co^{2+}, and Fe^{3+}) decorated Mn(II) doped 1D CdS NRs for photocatalytic hydrogen generation from water splitting. This is the first report of Mn(II) dopants utilized as charge transport bridges in non-noble metal co-catalysts for CdS-based photocatalysts. We also report the first use of $Fe(OH)_3$ as a co-catalyst for CdS. The energy transfer from 1D CdS host NRs to a long lifetime bridging Mn^{2+} ions followed by electron transfer to the self-regulating $M(OH)_x/M(0)$ redox couple on the surface of the Mn:CdS-$M(OH)_x$ NRs prevents fast charge recombination in the host CdS NRs. Crucially, during photocatalysis, $Ni(OH)_2$ has the highest performance at neutral (pH = 7) while $Co(OH)_2$, and $Fe(OH)_3$ had the highest rate of photocatalysis at higher pH values (>13). While neutral pH operation is desirable for practical water-splitting systems, the results presented here provide fundamental insights into charge-transfer processes and design principles for noble-metal-free co-catalysts. The higher rates of photocatalysis can be explained by a change in the thermodynamically stable phase of the metal hydroxide as revealed by Pourbaix diagram(s). Significant enhancement of the photocatalytic hydrogen generation rates came from the addition of Mn(II) dopants with noble metal free $M(OH)_x$ co-catalyst islands to the CdS NRs of 109.2 times (112.0 mmol g^{-1} h^{-1}), 7.3 times (59.5 mmol g^{-1} h^{-1}), and 6.8 times (56.1 mmol g^{-1} h^{-1}), for Mn:CdS-$Ni(OH)_2$, Mn:CdS-$Co(OH)_2$, and Mn:CdS-$Fe(OH)_3$, respectively. Introducing noble metal free co-catalysts can provide new opportunities for both efficient charge separation and active sites in high performance photocatalysts for wide range industry applications.

Conflicts of interest

There are no conflicts to declare.

Data availability

The authors confirm that all data supporting the findings of this study are available within the article and its supplementary information (SI). Supplementary information: experimental details for control experiments; structural and optical characterization of 1D CdS-based NRs; electrochemical measurements; and photocatalytic water-splitting studies. See DOI: https://doi.org/10.1039/d5ta08886k.

Acknowledgements

The research is sponsored by the Department of Chemistry and the Center of Excellence in Environmental and Energy Systems at Syracuse University.

References

1 H. Lv, T. P. A. Ruberu, V. E. Fleischauer, W. W. Brennessel, M. L. Neidig and R. Eisenberg, Catalytic Light-Driven Generation of Hydrogen from Water by Iron Dithiolene Complexes, *J. Am. Chem. Soc.*, 2016, **138**(36), 11654–11663.
2 L. Xu, M. Chen, P. Hou, X. Hou, J. Wang, Q. Qi, Y. Zhu, X. Yang, X. Liu, X. Li, G. Jia, S. Zhang and J. Du, Synthesis of CdSe Nanowires and $CuInSe_2$ Nanosheets for Hydrogen Evolution, *ACS Appl. Nano Mater.*, 2022, **5**(2), 1935–1943.
3 W. D. Kim, J.-H. Kim, S. Lee, S. Lee, J. Y. Woo, K. Lee, W.-S. Chae, S. Jeong, W. K. Bae, J. A. McGuire, J. H. Moon, M. S. Jeong and D. C. Lee, Role of Surface States in Photocatalysis: Study of Chlorine-Passivated CdSe Nanocrystals for Photocatalytic Hydrogen Generation, *Chem. Mater.*, 2016, **28**(3), 962–968.
4 P. Fatahi, A. Roy, M. Bahrami and S. J. Hoseini, Visible-Light-Driven Efficient Hydrogen Production from CdS NanoRods Anchored with Co-catalysts Based on Transition Metal Alloy Nanosheets of NiPd, NiZn, and NiPdZn, *ACS Appl. Energy Mater.*, 2018, **1**(10), 5318–5327.
5 W. Yang, Q. Peng, H. Yang, X. Li, J. Cao, J. Wang, Y. Zheng, C. Li and J. Pan, Hollow Co_3O_4/CdS Nanoparticles for Photocatalytic Hydrogen Evolution and Photodegradation, *ACS Appl. Nano Mater.*, 2024, **7**(16), 18157–18166.
6 W. MacSwain, D.-K. Ma, Z.-J. Li, H. Lin, Y.-L. Bai, X. Hu and W. Zheng, Metal-based co-catalysts in semiconductor CdS hybrid nanostructures for enhanced photocatalysis: material design, mechanisms, and emerging trends, *Coord. Chem. Rev.*, 2026, **549**, 217247.
7 J. Yu, Y. Yu, P. Zhou, W. Xiao and B. Cheng, Morphology-dependent photocatalytic H_2-production activity of CdS, *Appl. Catal., B*, 2014, **156–157**, 184–191.
8 J. Yuan, J. Wen, Q. Gao, S. Chen, J. Li, X. Li and Y. Fang, Amorphous Co_3O_4 modified CdS nanorods with enhanced visible-light photocatalytic H_2-production activity, *Dalton Trans.*, 2015, **44**(4), 1680–1689.
9 J. A. Nasir, Z. U. Rehman, S. N. A. Shah, A. Khan, I. S. Butler and C. R. A. Catlow, Recent developments and perspectives in CdS-based photocatalysts for water splitting, *J. Mater. Chem. A*, 2020, **8**(40), 20752–20780.
10 J. S. Jang, U. A. Joshi and J. S. Lee, Solvothermal Synthesis of CdS Nanowires for Photocatalytic Hydrogen and Electricity Production, *J. Phys. Chem. C*, 2007, **111**(35), 13280–13287.
11 Q. Li, F. Zhao, C. Qu, Q. Shang, Z. Xu, L. Yu, J. R. McBride and T. Lian, Two-Dimensional Morphology Enhances Light-Driven H_2 Generation Efficiency in CdS Nanoplatelet-Pt Heterostructures, *J. Am. Chem. Soc.*, 2018, **140**(37), 11726–11734.
12 W. MacSwain, H. Lin, Z.-J. Li, S. Li, C. Chu, L. Dube, O. Chen, G. Leem and W. Zheng, Facilitated electron

transfer by Mn dopants in 1-dimensional CdS nanorods for enhanced photocatalytic hydrogen generation, *J. Mater. Chem. A*, 2023, **11**(13), 7066–7076.

13 K. Wu, Z. Chen, H. Lv, H. Zhu, C. L. Hill and T. Lian, Hole removal rate limits photodriven H_2 generation efficiency in CdS-Pt and CdSe/CdS-Pt semiconductor nanorod-metal tip heterostructures, *J. Am. Chem. Soc.*, 2014, **136**(21), 7708–7716.

14 S. Corby, R. R. Rao, L. Steier and J. R. Durrant, The kinetics of metal oxide photoanodes from charge generation to catalysis, *Nat. Rev. Mater.*, 2021, **6**(12), 1136–1155.

15 J. Wang, L. Xiong, Y. Bai, Z. Chen, Q. Zheng, Y. Shi, C. Zhang, G. Jiang and Z. Li, Mn-Doped Perovskite Nanocrystals for Photocatalytic CO_2 Reduction: Insight into the Role of the Charge Carriers with Prolonged Lifetime, *Sol. RRL*, 2022, **6**(8), 2200294.

16 Y. Zhu, Y. Wang, Z. Chen, L. Qin, L. Yang, L. Zhu, P. Tang, T. Gao, Y. Huang, Z. Sha and G. Tang, Visible light induced photocatalysis on CdS quantum dots decorated TiO_2 nanotube arrays, *Appl. Catal., A*, 2015, **498**, 159–166.

17 K. Rafiq, M. Sabir, M. Z. Abid, M. Jalil, M. A. Nadeem, S. Iqbal, A. Rauf and E. Hussain, Tuning of TiO_2/CdS Hybrid Semiconductor with Au Cocatalysts: State-of-the-Art Design for Sunlight-Driven H_2 Generation from Water Splitting, *Energy Fuels*, 2024, **38**(5), 4625–4636.

18 Z. Chen, D. Li and C. Chen, Urchin-like TiO_2/CdS Nanoparticles Forming an S-scheme Heterojunction for Photocatalytic Hydrogen Production and CO_2 Reduction, *ACS Appl. Nano Mater.*, 2023, **6**(23), 21897–21908.

19 X. Wang, G. Liu, L. Wang, Z. G. Chen, G. Q. Lu and H. M. Cheng, ZnO–CdS@Cd Heterostructure for Effective Photocatalytic Hydrogen Generation, *Adv. Energy Mater.*, 2012, **2**(1), 42–46.

20 D. Ma, Z. Wang, J.-W. Shi, Y. Zou, Y. Lv, X. Ji, Z. Li, Y. Cheng and L. Wang, An ultrathin Al_2O_3 bridging layer between CdS and ZnO boosts photocatalytic hydrogen production, *J. Mater. Chem. A*, 2020, **8**(21), 11031–11042.

21 Y. G. Kim and W.-K. Jo, Photodeposited-metal/CdS/ZnO heterostructures for solar photocatalytic hydrogen production under different conditions, *Int. J. Hydrogen Energy*, 2017, **42**(16), 11356–11363.

22 S. Sultana, S. Mansingh, M. Scurrell and K. M. Parida, Controlled Synthesis of CeO_2NS-Au-CdS QDs Ternary Nanoheterostructure: A Promising Visible Light Responsive Photocatalyst for H_2 Evolution, *Inorg. Chem.*, 2017, **56**(20), 12297–12307.

23 S. Ijaz, M. F. Ehsan, M. N. Ashiq, N. Karamat and T. He, Preparation of CdS@CeO_2 core/shell composite for photocatalytic reduction of CO_2 under visible-light irradiation, *Appl. Surf. Sci.*, 2016, **390**, 550–559.

24 K. Wu, Z. Chen, H. Lv, H. Zhu, C. L. Hill and T. Lian, Hole Removal Rate Limits Photodriven H_2 Generation Efficiency in CdS-Pt and CdSe/CdS-Pt Semiconductor Nanorod–Metal Tip Heterostructures, *J. Am. Chem. Soc.*, 2014, **136**(21), 7708–7716.

25 V. M. Daskalaki, M. Antoniadou, G. Li Puma, D. I. Kondarides and P. Lianos, Solar Light-Responsive Pt/CdS/TiO_2 Photocatalysts for Hydrogen Production and Simultaneous Degradation of Inorganic or Organic Sacrificial Agents in Wastewater, *Environ. Sci. Technol.*, 2010, **44**(19), 7200–7205.

26 J. Li, S. K. Cushing, P. Zheng, T. Senty, F. Meng, A. D. Bristow, A. Manivannan and N. Wu, Solar Hydrogen Generation by a CdS-Au-TiO_2 Sandwich Nanorod Array Enhanced with Au Nanoparticle as Electron Relay and Plasmonic Photosensitizer, *J. Am. Chem. Soc.*, 2014, **136**(23), 8438–8449.

27 S.-I. Naya, T. Kume, R. Akashi, M. Fujishima and H. Tada, Red-Light-Driven Water Splitting by Au(Core)–CdS(Shell) Half-Cut Nanoegg with Heteroepitaxial Junction, *J. Am. Chem. Soc.*, 2018, **140**(4), 1251–1254.

28 R. K. Chava, Y. Im and M. Kang, Internal electric field promoted charge separation via bismuth-based ternary heterojunctions with near-infrared light harvesting properties for efficient photoredox reactions, *J. Mater. Chem. A*, 2024, **12**(29), 18498–18511.

29 R. K. Chava, N. Son and M. Kang, Controllable oxygen doping and sulfur vacancies in one dimensional CdS nanorods for boosted hydrogen evolution reaction, *J. Alloys Compd.*, 2021, **873**, 159797.

30 R. K. Chava, J. Y. Do and M. Kang, Enhanced photoexcited carrier separation in CdS–SnS_2 heteronanostructures: a new 1D–0D visible-light photocatalytic system for the hydrogen evolution reaction, *J. Mater. Chem. A*, 2019, **7**(22), 13614–13628.

31 Y. Chen, W. Zhong, F. Chen, P. Wang, J. Fan and H. Yu, Photoinduced self-stability mechanism of CdS photocatalyst: The dependence of photocorrosion and H_2-evolution performance, *J. Mater. Sci. Technol.*, 2022, **121**, 19–27.

32 Y. Liu, S. Ding, Y. Shi, X. Liu, Z. Wu, Q. Jiang, T. Zhou, N. Liu and J. Hu, Construction of CdS/CoO_x core-shell nanorods for efficient photocatalytic H_2 evolution, *Appl. Catal., B*, 2018, **234**, 109–116.

33 X. Ning, J. Li, B. Yang, W. Zhen, Z. Li, B. Tian and G. Lu, Inhibition of photocorrosion of CdS via assembling with thin film TiO_2 and removing formed oxygen by artificial gill for visible light overall water splitting, *Appl. Catal., B*, 2017, **212**, 129–139.

34 V. Kumar, N. Singh, S. Jana, S. K. Rout, R. K. Dey and G. P. Singh, Surface polar charge induced Ni loaded CdS heterostructure nanorod for efficient photo-catalytic hydrogen evolution, *Int. J. Hydrogen Energy*, 2021, **46**(30), 16373–16386.

35 L. Zhang, X. Zhu, Y. Zhao, P. Zhang, J. Chen, J. Jiang and T. Xie, The photogenerated charge characteristics in Ni@NiO/CdS hybrids for increased photocatalytic H_2 generation, *RSC Adv.*, 2019, **9**(68), 39604–39610.

36 J. Ran, J. Yu and M. Jaroniec, $Ni(OH)_2$ modified CdS nanorods for highly efficient visible-light-driven photocatalytic H2 generation, *Green Chem.*, 2011, **13**(10), 2708.

37 Y.-Z. Lin, K. Wang, Y. Zhang, Y.-C. Dou, Y.-J. Yang, M.-L. Xu, Y. Wang, F.-T. Liu and K. Li, Metal–organic framework-

derived CdS–NiO heterostructures with modulated morphology and enhanced photocatalytic hydrogen evolution activity in pure water, *J. Mater. Chem. C*, 2020, **8**(29), 10071–10077.

38 X. Chen, W. Chen, H. Gao, Y. Yang and W. Shangguan, In situ photodeposition of NiO_X on CdS for hydrogen production under visible light: Enhanced activity by controlling solution environment, *Appl. Catal., B*, 2014, **152–153**, 68–72.

39 J. Li, X. Qian, Y. Peng and J. Lin, Hierarchical structure NiO/CdS for highly performance H_2 evolution, *Mater. Lett.*, 2018, **224**, 82–85.

40 Z. Khan, M. Khannam, N. Vinothkumar, M. De and M. Qureshi, Hierarchical 3D NiO–CdS heteroarchitecture for efficient visible light photocatalytic hydrogen generation, *J. Mater. Chem.*, 2012, **22**(24), 12090.

41 S. Qiao, C. Feng, Y. Guo, T. Chen, N. Akram, Y. Zhang, W. Wang, F. Yue and J. Wang, CdS nanoparticles modified Ni@NiO spheres as photocatalyst for oxygen production in water oxidation system and hydrogen production in water reduction system, *Chem. Eng. J.*, 2020, **395**, 125068.

42 L. Wang, H. Wei, Y. Fan, X. Gu and J. Zhan, One-Dimensional CdS/α-Fe_2O_3 and CdS/Fe_3O_4 Heterostructures: Epitaxial and Nonepitaxial Growth and Photocatalytic Activity, *J. Phys. Chem. C*, 2009, **113**(32), 14119–14125.

43 Z. Yan, X. Yu, A. Han, P. Xu and P. Du, Noble-Metal-Free $Ni(OH)_2$-Modified CdS/Reduced Graphene Oxide Nanocomposite with Enhanced Photocatalytic Activity for Hydrogen Production under Visible Light Irradiation, *J. Phys. Chem. C*, 2014, **118**(40), 22896–22903.

44 H. Lee, D. A. Reddy, Y. Kim, S. Y. Chun, R. Ma, D. P. Kumar, J. K. Song and T. K. Kim, Drastic Improvement of 1D-CdS Solar-Driven Photocatalytic Hydrogen Evolution Rate by Integrating with NiFe Layered Double Hydroxide Nanosheets Synthesized by Liquid-Phase Pulsed-Laser Ablation, *ACS Sustain. Chem. Eng.*, 2018, **6**(12), 16734–16743.

45 L. Mao, Q. Ba, S. Liu, X. Jia, H. Liu, W. Chen and X. Li, Pt–Ni_x alloy nanoparticles: a new strategy for cocatalyst design on a CdS surface for photo-catalytic hydrogen generation, *RSC Adv.*, 2018, **8**(55), 31529–31537.

46 L. Xie, J.-G. Hao, H.-Q. Chen, Z.-X. Li, S.-Y. Ge, Y. Mi, K. Yang and K.-Q. Lu, Recent advances of nickel hydroxide-based cocatalysts in heterogeneous photocatalysis, *Catal. Commun.*, 2022, **162**, 106371.

47 Y. Zhang, J. Wang, N. Xu, X. Wang and W. Su, $Ni(OH)_2$ modified $Mn_{0.5}Cd_{0.5}S$ with efficient photocatalytic H_2 evolution activity under visible-light, *Int. J. Hydrogen Energy*, 2020, **45**(41), 21532–21539.

48 M. Li, F. Chen, Y. Xu and M. Tian, $Ni(OH)_2$ Nanosheet as an Efficient Cocatalyst for Improved Photocatalytic Hydrogen Evolution over $Cd_{0.9}Zn_{0.1}S$ Nanorods under Visible Light, *Langmuir*, 2024, **40**(7), 3793–3803.

49 X. Wang, X. Zhang, W. Gao, Y. Sang, Y. Wang and H. Liu, Self-reduction derived nickel nanoparticles in CdS/$Ni(OH)_2$ heterostructure for enhanced photocatalytic hydrogen evolution, *J. Chem. Phys.*, 2020, **152**(21), 214701.

50 H. Zhang, X. Kong, F. Yu, Y. Wang, C. Liu, L. Yin, J. Huang and Q. Feng, $Ni(OH)_2$ Nanosheets Modified Hexagonal Pyramid CdS Formed Type II Heterojunction Photocatalyst with High-Visible-Light H_2 Evolution, *ACS Appl. Energy Mater.*, 2021, **4**(11), 13152–13160.

51 X. Zhou, J. Jin, X. Zhu, J. Huang, J. Yu, W.-Y. Wong and W.-K. Wong, New $Co(OH)_2$/CdS nanowires for efficient visible light photocatalytic hydrogen production, *J. Mater. Chem. A*, 2016, **4**(14), 5282–5287.

52 Y. Xu, Z. Xie, R. Yu, M. Chen and D. Jiang, $Co(OH)_2$ water oxidation cocatalyst-decorated CdS nanowires for enhanced photocatalytic CO_2 reduction performance, *Dalton Trans.*, 2021, **50**(29), 10159–10167.

53 J. Ran, J. Yu and M. Jaroniec, $Ni(OH)_2$ modified CdS nanorods for highly efficient visible-light-driven photocatalytic H_2 generation, *Green Chem.*, 2011, **13**(10), 2708–2713.

54 Z. Yan, X. Yu, Y. Zhang, H. Jia, Z. Sun and P. Du, Enhanced visible light-driven hydrogen production from water by a noble-metal-free system containing organic dye-sensitized titanium dioxide loaded with nickel hydroxide as the cocatalyst, *Appl. Catal., B*, 2014, **160–161**, 173–178.

55 D. Lang, F. Cheng and Q. Xiang, Enhancement of photocatalytic H_2 production activity of CdS nanorods by cobalt-based cocatalyst modification, *Catal. Sci. Technol.*, 2016, **6**(16), 6207–6216.

56 J. Wang, Y. Li, Q. Shen, T. Izuishi, Z. Pan, K. Zhao and X. Zhong, Mn doped quantum dot sensitized solar cells with power conversion efficiency exceeding 9%, *J. Mater. Chem. A*, 2016, **4**(3), 877–886.

57 Y. Dong, J. Choi, H.-K. Jeong and D. H. Son, Hot Electrons Generated from Doped Quantum Dots via Upconversion of Excitons to Hot Charge Carriers for Enhanced Photocatalysis, *J. Am. Chem. Soc.*, 2015, **137**(16), 5549–5554.

58 W. Li, D.-K. Ma, X. Hu, F. Gou, X. Yang, W. MacSwain, C. Qi and W. Zheng, General strategy for enhanced CH_4 selectivity in photocatalytic CO_2 reduction reactions by surface oxophilicity engineering, *J. Catal.*, 2022, **415**, 77–86.

59 W. Zheng, Z. Wang, J. Wright, B. Goundie, N. S. Dalal, R. W. Meulenberg and G. F. Strouse, Probing the Local Site Environments in Mn:CdSe Quantum Dots, *J. Phys. Chem. C*, 2011, **115**(47), 23305–23314.

60 M. Liu, Y. Du, L. Ma, D. Jing and L. Guo, Manganese doped cadmium sulfide nanocrystal for hydrogen production from water under visible light, *Int. J. Hydrogen Energy*, 2012, **37**(1), 730–736.

61 Z. Pan, S. Wang, R. Yan, C. Song, Y. Jin, G. Huang and J. Huang, Enhanced photocatalytic properties of Mn doped CdS catalysts by decomposition of complex precursors, *Opt. Mater.*, 2020, **109**, 110324.

62 H.-Y. Chen, S. Maiti and D. H. Son, Doping Location-Dependent Energy Transfer Dynamics in Mn-Doped CdS/ZnS Nanocrystals, *ACS Nano*, 2012, **6**(1), 583–591.

63 Z.-J. Li, E. Hofman, A. Blaker, A. H. Davis, B. Dzikovski, D.-K. Ma and W. Zheng, Interface Engineering of Mn-Doped ZnSe-Based Core/Shell Nanowires for Tunable

Host–Dopant Coupling, *ACS Nano*, 2017, **11**(12), 12591–12600.

64 S. Li, H. Lin, C. Chu, C. Martin, W. MacSwain, R. W. Meulenberg, J. M. Franck, A. Chakraborty and W. Zheng, Interfacial B-Site Ion Diffusion in All-Inorganic Core/Shell Perovskite Nanocrystals, *ACS Nano*, 2023, **17**(22), 22467–22477.

65 A. H. Davis, E. Hofman, K. Chen, Z.-J. Li, A. Khammang, H. Zamani, J. M. Franck, M. M. Maye, R. W. Meulenberg and W. Zheng, Exciton Energy Shifts and Tunable Dopant Emission in Manganese-Doped Two-Dimensional CdS/ZnS Core/Shell Nanoplatelets, *Chem. Mater.*, 2019, **31**(7), 2516–2523.

66 Z.-J. Li, E. Hofman, A. H. Davis, A. Khammang, J. T. Wright, B. Dzikovski, R. W. Meulenberg and W. Zheng, Complete Dopant Substitution by Spinodal Decomposition in Mn-Doped Two-Dimensional CsPbCl3 Nanoplatelets, *Chem. Mater.*, 2018, **30**(18), 6400–6409.

67 Z.-J. Li, S. Li, A. H. Davis, E. Hofman, G. Leem and W. Zheng, Enhanced singlet oxygen generation by hybrid Mn-doped nanocomposites for selective photo-oxidation of benzylic alcohols, *Nano Res.*, 2020, **13**(6), 1668–1676.

68 A. E. Saunders, A. Ghezelbash, P. Sood and B. A. Korgel, Synthesis of High Aspect Ratio Quantum-Size CdS Nanorods and Their Surface-Dependent Photoluminescence, *Langmuir*, 2008, **24**(16), 9043–9049.

69 J. S. Chen, T. Zhu, Q. H. Hu, J. Gao, F. Su, S. Z. Qiao and X. W. Lou, Shape-Controlled Synthesis of Cobalt-based Nanocubes, Nanodiscs, and Nanoflowers and Their Comparative Lithium-Storage Properties, *ACS Appl. Mater. Interfaces*, 2010, **2**(12), 3628–3635.

70 L. J. Zhang, R. Zheng, S. Li, B. K. Liu, D. J. Wang, L. L. Wang and T. F. Xie, Enhanced Photocatalytic H_2 Generation on Cadmium Sulfide Nanorods with Cobalt Hydroxide as Cocatalyst and Insights into Their Photogenerated Charge Transfer Properties, *ACS Appl. Mater. Interfaces*, 2014, **6**(16), 13406–13412.

71 Z. Zhao, H. Zhang, P. Chen, G. Jin and L. Wu, $Fe(OH)_3$/$Ti_3C_2T_x$ nanocomposites for enhanced ammonia gas sensor at room temperature, *Nanotechnology*, 2024, **35**(50), 505502.

72 G. Nagaraju, Y. H. Ko and J. S. Yu, Self-assembled hierarchical β-cobalt hydroxide nanostructures on conductive textiles by one-step electrochemical deposition, *CrystEngComm*, 2014, **16**(48), 11027–11034.

73 A. J. Yost, T. K. Ekanayaka, G. Gurung, G. Rimal, S. Horoz, J. Tang, T. Paudel and T. Chien, Influence of the Cation on the Surface Electronic Band Structure and Magnetic Properties of Mn:ZnS and Mn:CdS Quantum Dot Thin Films, *J. Phys. Chem. C*, 2019, **123**(40), 24890–24898.

74 J. Zhao, Z. Lu, X. He, X. Zhang, Q. Li, T. Xia, W. Zhang and C. Lu, Fabrication and Characterization of Highly Porous $Fe(OH)_3$@Cellulose Hybrid Fibers for Effective Removal of Congo Red from Contaminated Water, *ACS Sustain. Chem. Eng.*, 2017, **5**(9), 7723–7732.

75 M. Abdelmoula, C. Ruby, M. Mallet, J. Ghanbaja, R. Coustel, L. Scudiero and W.-J. Wang, Identification of a $Fe(OH)_2$-like phase in the core–shell structure of nano-zero-valent Fe and its evolution when interacting with Pd_{aq}^{2+} ions by Mössbauer spectroscopy, XPS, and TEM, *J. Phys. Chem. Solids*, 2023, **172**, 111066.

76 L. Wang, H. Zhang, Y. Li, S. Xiao, F. Bi, L. Zhao, G. Gai and X. Yang, Construction of bundle-like cobalt/nickel hydroxide nanorods from metal organic framework for high-performance supercapacitors, *J. Mater. Sci.: Mater. Electron.*, 2022, **33**(13), 10540–10550.

77 X. Li, K. Patil, A. Agarwal, P. Babar, J. S. Jang, X. Chen, Y. T. Yoo and J. H. Kim, $Ni(OH)_2$ Coated CoMn-layered double hydroxide nanowires as efficient water oxidation electrocatalysts, *New J. Chem.*, 2022, **46**(5), 2044–2052.

78 A. Kudielka, M. Schmid, B. P. Klein, C. Pietzonka, J. M. Gottfried and B. Harbrecht, Nanocrystalline cobalt hydroxide oxide: Synthesis and characterization with SQUID, XPS, and NEXAFS, *J. Alloys Compd.*, 2020, **824**, 153925.

79 E. Hofman, R. J. Robinson, Z.-J. Li, B. Dzikovski and W. Zheng, Controlled Dopant Migration in CdS/ZnS Core/Shell Quantum Dots, *J. Am. Chem. Soc.*, 2017, **139**(26), 8878–8885.

80 C. Chu, E. Hofman, C. Gao, S. Li, H. Lin, W. MacSwain, J. M. Franck, R. W. Meulenberg, A. Chakraborty and W. Zheng, Inserting an "atomic trap" for directional dopant migration in core/multi-shell quantum dots, *Chem. Sci.*, 2023, **14**(48), 14115–14123.

81 E. Hofman, A. Khammang, J. T. Wright, Z.-J. Li, P. F. McLaughlin, A. H. Davis, J. M. Franck, A. Chakraborty, R. W. Meulenberg and W. Zheng, Decoupling and Coupling of the Host–Dopant Interaction by Manipulating Dopant Movement in Core/Shell Quantum Dots, *J. Phys. Chem. Lett.*, 2020, **11**(15), 5992–5999.

82 W. He, X. Li, S. An, T. Li, Y. Zhang and J. Cui, 3D β-$Ni(OH)_2$ nanowires/RGO composite prepared by phase transformation method for superior electrochemical performance, *Sci. Rep.*, 2019, **9**(1), 10838.

83 Š. Trafela, J. Zavašnik, S. Šturm and K. Ž. Rožman, Formation of a $Ni(OH)_2$/NiOOH active redox couple on nickel nanowires for formaldehyde detection in alkaline media, *Electrochim. Acta*, 2019, **309**, 346–353.

84 R.-C. Xie, C. Batchelor-McAuley, E. Rauwel, P. Rauwel and R. G. Compton, Electrochemical Characterisation of Co@$Co(OH)_2$ Core-Shell Nanoparticles and their Aggregation in Solution, *ChemElectroChem*, 2020, **7**(20), 4259–4268.

85 K. Duschek, M. Uhlemann, H. Schlörb, K. Nielsch and K. Leistner, Electrochemical and in situ magnetic study of iron/iron oxide films oxidized and reduced in KOH solution for magneto-ionic switching, *Electrochem. Commun.*, 2016, **72**, 153–156.

86 M. J. N. Pourbaix, *Atlas of Electrochemical Equilibria in Aqueous Solutions*, 1974.

87 L. F. Huang, M. J. Hutchison, R. J. Santucci, Jr, J. R. Scully and J. M. Rondinelli, Improved Electrochemical Phase Diagrams from Theory and Experiment: The Ni–Water

System and Its Complex Compounds, *J. Phys. Chem. C*, 2017, **121**(18), 9782–9789.

88 J. Chivot, L. Mendoza, C. Mansour, T. Pauporté and M. Cassir, New insight in the behaviour of Co–H_2O system at 25–150 °C, based on revised Pourbaix diagrams, *Corros. Sci.*, 2008, **50**(1), 62–69.

89 E. M. Garcia, J. S. Santos, E. C. Pereira and M. B. J. G. Freitas, Electrodeposition of cobalt from spent Li-ion battery cathodes by the electrochemistry quartz crystal microbalance technique, *J. Power Sources*, 2008, **185**(1), 549–553.

90 D. Okumusoglu and O. Gündüz, Hydrochemical Status of an Acidic Mining Lakein Çan-Çanakkale, Turkey, *Water Environ. Res.*, 2013, **85**(7), 604–620.

91 H. Weinrich, Y. E. Durmus, H. Tempel, H. Kungl and R.-A. Eichel, Silicon and Iron as Resource-Efficient Anode Materials for Ambient-Temperature Metal-Air Batteries: A Review, *Materials*, 2019, **12**(13), 2134.

92 H. S. Belson, Shiftless Fermi Level in Iron, Nickel, and Cobalt, *J. Appl. Phys.*, 1966, **37**(3), 1348–1349.

93 M. D. Scanlon, P. Peljo, M. A. Méndez, E. Smirnov and H. H. Girault, Charging and discharging at the nanoscale: Fermi level equilibration of metallic nanoparticles, *Chem. Sci.*, 2015, **6**(5), 2705–2720.

94 H. Reiss, The Fermi level and the redox potential, *J. Phys. Chem.*, 1985, **89**(18), 3783–3791.

95 B. P. Mishra, J. Dahiya and V. Krishnan, Semiconductor photocatalysts for hydrogen evolution: critical role of cocatalysts in enhancing performance, *Chem. Commun.*, 2025, **61**(89), 17302–17329.

96 Z.-J. Li, J.-J. Wang, X.-B. Li, X.-B. Fan, Q.-Y. Meng, K. Feng, B. Chen, C.-H. Tung and L.-Z. Wu, An Exceptional Artificial Photocatalyst, Ni_h-CdSe/CdS Core/Shell Hybrid, Made In Situ from CdSe Quantum Dots and Nickel Salts for Efficient Hydrogen Evolution, *Adv. Mater.*, 2013, **25**(45), 6613–6618.

97 T. Simon, N. Bouchonville, M. J. Berr, A. Vaneski, A. Adrović, D. Volbers, R. Wyrwich, M. Döblinger, A. S. Susha, A. L. Rogach, F. Jäckel, J. K. Stolarczyk and J. Feldmann, Redox shuttle mechanism enhances photocatalytic H_2 generation on Ni-decorated CdS nanorods, *Nat. Mater.*, 2014, **13**(11), 1013–1018.

98 L. A. Silva, S. Y. Ryu, J. Choi, W. Choi and M. R. Hoffmann, Photocatalytic Hydrogen Production with Visible Light over Pt-Interlinked Hybrid Composites of Cubic-Phase and Hexagonal-Phase CdS, *J. Phys. Chem. C*, 2008, **112**(32), 12069–12073.

99 Z. Wang and A. Meijerink, Concentration Quenching in Upconversion Nanocrystals, *J. Phys. Chem. C*, 2018, **122**(45), 26298–26306.

100 J. Cao, J. Yang, Y. Zhang, L. Yang, Y. Wang, M. Wei, Y. Liu, M. Gao, X. Liu and Z. Xie, Optimized doping concentration of manganese in zinc sulfide nanoparticles for yellow-orange light emission, *J. Alloys Compd.*, 2009, **486**(1–2), 890–894.